International Journal of Control
Vol. 00, No. 00, DD Month 200x, 1–32

International Journal of Control
2007, vol 80, pp 1912-1930

Linear Quadratic Control of Plane Poiseuille Flow - the Transient Behaviour

J.McKernan*† J. F. Whidborne‡ G. Papadakis§

(*May 2, 2007*)

This paper describes the design of optimal linear quadratic controllers for single wavenumber-pair periodic 2-D disturbances in plane Poiseuille flow, and subsequent verification using a finite-volume full Navier-Stokes solver, at both linear and non-linear levels of initial conditions selected to produce the largest linear transient energy growth. For linear magnitude initial conditions, open and closed-loop finite-volume solver results agree well with a linear simulation. Transient energy growth is an important performance measure in fluid flow problems. The controllers reduced the transient energy growth, and the non-linear effects are generally seen to keep energy levels below the scaled linear values, although they did cause instability in one simulation. Comparatively large local quantities of transpiration fluid are required. The modes responsible for the transient energy growth are identified. Modes are shown not to become significantly more orthogonal by the application of control. The synthesis of state estimators is shown to require higher levels of discretisation than the synthesis of state-feedback controllers. A simple tuning of the estimator weights is presented with improved convergence over uniform weights from zero initial estimates.

Keywords: Flow control, simulation, optimal linear quadratic control, full Navier-Stokes solver.

*†Cranfield University, MK43 0AL, UK (john.mckernan@btinternet.com)
‡Cranfield University, MK43 0AL, UK (j.f.whidborne@cranfield.ac.uk)
§King's College, London, WC2R 2LS, UK (george.papadakis@kcl.ac.uk)

Nomenclature

Greek Symbols

α	:=	streamwise(x) wave number, cycles per 2π distance
β	:=	spanwise(z) wave number, cycles per 2π distance
$\epsilon(t)$	:=	synchronic transient energy bound at time t
$\epsilon_{Error}(t)$	:=	synchronic error energy bound at time t
ζ	:=	eigenvalue in synchronic transient energy bound eigensystem
$\eta(x,y,z,t)$	:=	wall-normal vorticity perturbation
$\tilde{\eta}(\alpha,\beta,y,t) \in \mathbb{C}$	:=	η Fourier coefficient at wavenumber pair α,β
θ	:=	diachronic transient energy bound
θ_{Error}	:=	diachronic error energy bound
θ_{Est}	:=	estimated energy bound
$\lambda_i \in \mathbb{C}$	:=	i^{th} eigenvalue
$\Lambda \in \mathbb{C}^{M\times M}$	:=	diagonal eigenvalue matrix
μ	:=	molecular or kinematic viscosity
ρ	:=	fluid density
$\sigma_i(\mathbf{A})$	:=	i^{th} singular value of $\mathbf{A}$
$\bar{\sigma}(\mathbf{A})$	:=	spectral norm or largest singular value of $\mathbf{A}$
$\chi \in \mathbb{R}^M$	:=	modal amplitude vector, $[c_0,\ldots,c_M]^T$
χ_0	:=	initial χ, at time $t=0$
Ψ	:=	matrix of right eigenvectors
ψ_i	:=	i^{th} right eigenvector
$\omega \in \mathbb{C}$	:=	frequency

Roman Symbols

$\mathbf{A} \in \mathbb{R}^{M\times M}$	:=	system matrix
$\mathbf{B} \in \mathbb{R}^{M\times P}$	:=	input matrix
$\mathbf{C} \in \mathbb{R}^{Q\times M}$	:=	output matrix
$a_n \in \mathbb{C}$	:=	multiplying co-efficient for n^{th} Chebyshev polynomial
c_i	:=	amplitude of mode i
$E(t)$	:=	transient energy, $\mathbf{X}^T\mathbf{Q}\mathbf{X}$, at time t
$E_{Est}(t)$	:=	estimated transient energy, $\hat{\mathbf{X}}^T\mathbf{Q}\hat{\mathbf{X}}$, at time t
$E_{Error}(t)$	:=	error energy $\left(\mathbf{X}-\hat{\mathbf{X}}\right)^T\mathbf{Q}\left(\mathbf{X}-\hat{\mathbf{X}}\right)$, at time t
E_0	:=	E of worst open-loop perturbation of $\max v = 0.0001$, at $t = 0$
	:=	2.26×10^{-9}
$E_{pair,bound}$	:=	upper bound on mode pair energy growth
h	:=	channel wall separation
$\mathbf{I}$	:=	identity matrix
$\jmath$	:=	$\sqrt{-1}$
$\mathbf{K} \in \mathbb{R}^{P\times M}$	:=	state feedback gain matrix
$\mathbf{L} \in \mathbb{R}^{P\times M}$	:=	estimator gain matrix
N	:=	highest Chebyshev polynomial degree used, final collocation point index
P	:=	pressure
P_b	:=	steady base flow pressure
p	:=	pressure perturbation
$\mathbf{Q} \in \mathbb{R}^{M\times M}$	:=	state variable weighting (energy) matrix
$\mathbf{R} \in \mathbb{R}^{P\times P}$	:=	control weighting matrix
R	:=	Reynolds number
r	:=	control weight multiplier
s	:=	measurement noise weight multiplier
$\mathbf{T}_{cp} \in \mathbb{R}^{M\times M}$	:=	invertible matrix for conversion between state variables and $\tilde{v}, \tilde{\eta}$, excludes next-to-wall velocities and wall vorticities
t	:=	time
x, y, z	:=	streamwise, wall-normal and spanwise co-ordinates
$\vec{U} = (U, V, W)$	:=	flow velocity vector
$\vec{U}_b = (U_b, V_b, W_b)$	:=	steady base flow velocity
U_{cl}	:=	U_b at centreline
$\vec{u} = (u, v, w)$	:=	velocity perturbation vector
$\tilde{u}, \tilde{v}, \tilde{w} \in \mathbb{C}$	:=	u, v, w Fourier coefficients at wavenumber pair α, β
$\mathbf{U} \in \mathbb{R}^{M}$	:=	control vector
$\mathbf{V} \in \mathbb{R}^{Q\times Q}$	:=	measurement noise power spectral density
$\mathbf{W} \in \mathbb{R}^{M\times M}$	:=	process noise power spectral density
$\mathbf{X} \in \mathbb{R}^{M}$	:=	state variable vector
$\hat{\mathbf{X}} \in \mathbb{R}^{M}$	:=	state estimates vector
$\mathbf{X}_{Error} \in \mathbb{R}^{M}$	:=	estimate error vector, $\mathbf{X} - \hat{\mathbf{X}}$
$\mathbf{X}_{Worst} \in \mathbb{R}^{M}$	:=	$\mathbf{X}(t = 0)$ which generates θ
$\mathbf{X}_{Error,Worst} \in \mathbb{R}^{M}$	:=	$\mathbf{X}_{Error}(t = 0)$ which generates θ_{Error}
$\mathbf{X}_{cp} \in \mathbb{R}^{M}$	:=	$\mathbf{X}$ transformed to $\tilde{v}, \tilde{\eta}$ values at collocation points
$\tilde{\mathbf{X}} \in \mathbb{R}^{M}$	:=	state variables transformed to $\mathbf{Q}^{1/2}\mathbf{X}$, thus $E = \tilde{\mathbf{X}}^T\tilde{\mathbf{X}}$
$\mathbf{Y} \in \mathbb{R}^{Q}$	:=	measurement vector
y_n	:=	y at n^{th} Chebyshev-Gauss-Lobatto collocation point

1 Introduction

Laminar flow is characterised by a smooth flow-field in which adjacent layers of fluid undergo shear. Turbulent flow is characterised by an unsteady flow-field in which fluctuations of widely varying length and time scales cause large amounts of mixing between adjacent layers of fluid, in a self sustaining process. The transition of laminar fluid flow into turbulent flow results in large increases in fluid drag, and the prevention of transition would lead to substantial savings in the energy required to sustain the flow. The process of transition from laminar to turbulent flow is thought to begin with the rapid growth of small disturbances in laminar flow.

Plane Poiseuille or channel flow, the unidirectional flow between infinite parallel planes, is a simple flow that is prone to transition. Experiments show that this flow undergoes transition to turbulence for Reynolds number as low as 1000, for example as shown by Carlson et al. (1982).

Fluid flow-field velocity and pressure, and wall shear stresses, can be measured. The flow can be influenced by the manipulation of the conditions on its boundaries, such as the injection and suction of fluid at the walls, known as wall transpiration. This opens up the possibility of the control of the evolution of transition by the feedback control of flow measurements to suitable wall actuators. The governing Navier-Stokes and continuity equations can be used to develop plant models for the synthesis of controllers. Linear plant models are often based on spectral analysis of the linearized Navier-Stokes equations, e.g. as performed by Baramov et al. (2001), Bewley and Liu (1998), and Joshi et al. (1999).

Experiments to detect transition, even in such a simple flow, are difficult and expensive to perform, but computational fluid dynamics (CFD) has progressed to the stage where it can be used to simulate the performance of controllers. Baramov et al. (2001) used specialised finite-difference full Navier-Stokes solvers, and the widely cited work of Bewley et al. (2001) employed hybrid spectral finite-difference full Navier-Stokes solvers. However little use has been made of finite-volume CFD codes other than that by Balogh et al. (2000) testing low speed global Lyapunov stabilization, although their use is widespread in other fields, for example see Yeoh et al. (2004).

Although plane Poiseuille flow undergoes transition to turbulence for Reynolds number as low as 1000, it is known to be linearly stable at Reynolds numbers below approximately 5772, as calculated by Orszag (1971). The occurrence of transition in the linearly stable regime is thought to be due to large transient energy growth causing non-linear effects. Transient energy growth is the amplification of the kinetic energy contained in an initial perturbation. Trefethen et al. (1993) note that the large transient energy growth is itself due to non-normality of the system eigenvectors. Hinrichsen et al. (2002) have investigated state feedback stabilization with guaranteed transient bounds and Whidborne et al. (2005) have derived controllers which minimise maximum transient energy growth. Although non-normal behaviour is the cause of the transient growth, little is known regarding the pairs of modes involved.

This paper describes the synthesis of optimal linear quadratic controllers using a state-space model of plane Poiseuille flow. This work is not the first to use linear quadratic control for plane Poiseuille flow. Joshi et al. (1999) described the application of linear system theory to a stream function formulation of linearised plane Poiseuille flow, limited to streamwise/wall-normal disturbances. The paper by Bewley and Liu (1998) is seminal, and to some extent, the work described here is motivated by their results from investigations of control of a spectral linear velocity/vorticity model at a single wavenumber pair using an interpolating basis for wall-normal behaviour.

Here, in contrast to the approach of Bewley and Liu, the state-space model employs a polynomial wall-normal basis derived by McKernan (2006), which, using a rigorous application of the boundary conditions,

produces a system free of spurious eigenmodes, and leads to control via rate of change of wall-normal transpiration velocity. Furthermore, the transient energy matrix is rigorously derived, and tuned process noise covariance matrices are investigated. In addition, the controllers synthesized are subsequently tested in a full model of the flow, namely a finite-volume non-linear Navier-Stokes solver. Thus the controllers are tested using a well tried non-linear algorithm which is completely independent of the development model.

Like Bewley and Liu, a single wavenumber pair is controlled, and the pair selected represents streamwise vortices, which lead to the largest transient energy growth. These perturbations are streamwise constant, which allows the subsequent finite volume simulations to be two-dimensional.

Section 2 and 3 briefly introduce plane Poiseuille flow and the linear plant model. For a full derivation of the model see McKernan (2006). Section 4 describes the synthesis of optimal state feedback controllers and optimal state estimators. The controllers are linear quadratic regulators (LQR), which are optimal in the sense of minimising a quadratic cost functional of the weighted state variables and control inputs. The estimators are linear quadratic estimators (LQE), which are optimal in the sense of minimising the expectation of the state estimation errors, given weighting matrices which represent the process and measurement noise covariances. The section also describes the selection of appropriate weighting matrices.

Section 5 describes the linear and non-linear simulations undertaken on the open- and closed-loop systems. The open-loop (OL) systems comprise the plant model with LQE state estimator and the closed-loop systems comprise the plant model with state feedback LQR control, and with output feedback linear quadratic Gaussian (LQG) control, the latter formed by employing both the LQE estimator and LQR controller. The section states the derivation of the worst initial conditions and the conditions for minimum transient energy growth, and derives plant modal and non-modal energy terms and an upper bound on mode pair energy growth.

Finally section 7 draws conclusions regarding the controller and estimator synthesis, and the controller and estimator performance in the linear and non-linear simulations.

2 Plane Poiseuille Flow Control

Incompressible fluid flow is described by the Navier-Stokes and continuity equations. The Navier-Stokes equations (1) form a set of three coupled, non-linear, partial differential equations representing conservation of momentum, and the continuity equation is an additional constraint representing the conservation of mass (2);-

$$\dot{\vec{U}} + \left(\vec{U} \cdot \nabla\right) \vec{U} = -\frac{1}{\rho}\nabla P + \frac{\mu}{\rho}\nabla^2 \vec{U} \tag{1}$$

$$\nabla \cdot \vec{U} = 0 \tag{2}$$

where $\vec{U}, P, \rho, \mu$ are velocity, pressure, density and viscosity respectively.

Laminar Poiseuille flow has a parabolic streamwise velocity profile, with no slip occurring at the bounding parallel planes. It undergoes transition to turbulence when small disturbances $\vec{u} = (u, v, w), p$ about the steady base profile, $\vec{U}_b = \left((1 - y^2)U_{cl}, 0, 0\right), P_b$, grow spatially and temporally to form a self-sustaining turbulent flow. If the equations for the perturbations are made non-dimensional by dividing length scales by the channel half height h, velocities by the base flow centreline velocity U_{cl}, and pressures by ρU_{cl}^2,

they become

$$\dot{\vec{u}} + \left(\vec{U}_b \cdot \nabla\right) \vec{u} + \left(\vec{u} \cdot \nabla\right) \vec{u} + \left(\vec{u} \cdot \nabla\right) \vec{U}_b = -\nabla p + \frac{1}{R} \nabla^2 \vec{u} \tag{3}$$

$$\nabla \cdot \vec{u} = 0 \tag{4}$$

where R is the dimensionless Reynolds number $\rho U_{cl} h / \mu$.

The no-slip wall boundary conditions in plane Poiseuille flow are replaced by prescribed wall transpiration velocities when boundary control is implemented, $(u(y = \pm 1) = 0, v(y = \pm 1) \neq 0, w(y = \pm 1) = 0)$.

In this paper, disturbances $\vec{u}$ which vary in the wall-normal (y) and spanwise (z) directions are investigated, with no variation in the streamwise direction (x). This paper also approximates the infinite extent of the flow by a periodic representation, such that the flow disturbances may only grow in time, but not in space.

3 Linear Plant Model

Boundary control of the linearized Navier-Stokes equations in a channel, assuming periodic behaviour at streamwise (x) and spanwise (z) wavenumbers α and β respectively, may be cast in state-space form as

$$\dot{\mathbf{X}} = \mathbf{A}\mathbf{X} + \mathbf{B}\mathbf{U}$$

$$\mathbf{Y} = \mathbf{C}\mathbf{X} \tag{5}$$

where the states $\mathbf{X}$ are wall-normal velocity $\tilde{v}$ and vorticity $\tilde{\eta}$ $(\partial u/\partial z - \partial w/\partial x)$ perturbation Chebyshev series coefficients a in the wall-normal direction (y), plus the upper and lower wall velocities $\tilde{v}_u$ and $\tilde{v}_l$ respectively

$$\mathbf{X} = \begin{pmatrix} a_{v,n=0,\ldots,N-4} \\ a_{\eta,n=0,\ldots,N-2} \\ \tilde{v}_u \\ \tilde{v}_l \end{pmatrix} \tag{5A}$$

where N is the discretisation parameter (for further details see McKernan, 2006, p36). The measurements $\mathbf{Y}$ are shear stresses on the upper and lower walls, and the inputs $\mathbf{U}$ are rates of change of transpiration velocity on the upper and lower walls. Since these are rates of change, the system contains two integrators, each with an eigenvector representing steady state transpiration from a wall. This situation arises since, for this linearised flow model, steady transpiration at a set velocity merely superimposes a velocity flow field on the existing perturbation. Only by varying the transpiration velocity does the existing perturbation flow field change dynamically.

The coefficients of the Chebyshev series, shear measurements and transpiration velocity are complex since they convey the spatial phase of the wavenumber pair perturbations, but the state-space system is here made real-valued by decomposing them into their real- and imaginary-valued parts (Hinrichsen and Pritchard, 2005, p720). The test case considered here is $\alpha = 0, \beta = 2.044, R = 5000$. This test case is stable but has the largest diachronic transient energy bound, i.e. the largest linear transient energy growth

over all unit initial conditions, time and α, β, and represents the very earliest stages of the transition to turbulence. Modelling turbulence itself would involve using many more degrees of freedom. For a full derivation of the model see McKernan (2006).

4 Controller Synthesis

4.1 *Optimal State Feedback*

The standard LQR control problem states that given the open-loop system or 'plant', (5), the feedback control signal that minimizes;-

$$\int_0^\infty \left(\mathbf{X}(t)^T\mathbf{Q}\mathbf{X}(t) + \mathbf{U}(t)^T\mathbf{R}\mathbf{U}(t)\right) dt \tag{6}$$

is given by $\mathbf{U} = -\mathbf{K}\mathbf{X}$ where $\mathbf{K} = \mathbf{R}^{-1}\mathbf{B}^T\mathbf{P}$ and $\mathbf{P} = \mathbf{P}^T \geq 0$ is the solution of the algebraic Riccati equation

$$\mathbf{A}^T\mathbf{P} + \mathbf{P}\mathbf{A} - \mathbf{P}\mathbf{B}\mathbf{R}^{-1}\mathbf{B}^T\mathbf{P} + \mathbf{Q} = 0 \tag{7}$$

where $\mathbf{Q}$ and $\mathbf{R}$ are weighting matrices. The closed-loop state feedback LQR system is

$$\begin{aligned} \dot{\mathbf{X}} &= (\mathbf{A} - \mathbf{B}\mathbf{K})\,\mathbf{X} \\ \mathbf{Y} &= \mathbf{C}\mathbf{X} \end{aligned} \tag{8}$$

The state feedback controller $\mathbf{K}$ is the optimal for all initial conditions (Skogestad and Postlethwaite, 1996, p354).

In most problems the weighting matrices are tuned by hand. However, for a fluid system this is not practical because of the large number of state variables. Furthermore, it is useful to employ a weighting matrix $\mathbf{Q}$ that is defined independently of the chosen state-space basis since then there is freedom to alter either. It is also helpful if the weights are defined independently of the level of discretisation, in order to make interpretation of results easier, as recommended by Lauga and Bewley (2004). Bewley and Liu (1998) suggests that a natural choice for the matrix $\mathbf{Q}$ is such that $\mathbf{X}^T\mathbf{Q}\mathbf{X}$ represents the discretized form of the transient energy E,

$$E = \frac{1}{V}\int_{vol=V} \rho\frac{\vec{u}^T\vec{u}}{2}\, dvol \tag{9}$$

where E has dimensions energy per unit volume, and $\vec{u}$ is the perturbation velocity vector. This choice of $\mathbf{Q}$ is independent of the definition of the state variables, is independent (in the limiting case) of the discretisation N, and also means that the LQR problem (6) minimises E in some sense. This evaluation of the transient energy requires that the state variables remain physically meaningful, and thus model reduction is not possible.

Matrix Q effectively performs quadrature on the wall-normal velocity $\tilde{v}$, velocity derivative $\partial\tilde{v}/\partial y$ and vorticity $\tilde{\eta}$ values at the collocation (discretisation) points across the channel. The state variables and thus the energy matrix employed in this paper are based on a polynomial Chebyshev form with the channel wall and next-to-wall Navier-Stokes equations omitted,

and the highest order Chebyshev series coefficients a (5A) discarded, as required during the application of the boundary conditions, as described in McKernan (2006). The velocity derivatives are obtained via well-behaved algebraic differentiation of the Chebyshev series. The polynomial form is amenable to the coefficient discarding described above, due to the spectral decay of the coefficients, and analytical and numerical tests validate the expression used here for Q on distributions of velocity and vorticity which fulfill the open- and closed-loop boundary conditions.

The state variables and energy matrix derived by Bewley and Liu (1998, p312) are based on an interpolating Chebyshev form with the channel wall values omitted. Quadrature on velocity and vorticity values in the open-loop case when the wall values are zero is appropriate, and a small approximation in their contribution to the transient energy occurs when the wall-velocity is non-zero in the closed-loop case, as some energy very close to the wall is neglected. However, omitting the channel wall values in the closed-loop case, when the wall velocity values are not zero, leads to the interpolating form assuming zero wall values, and this produces well-known high order interpolation oscillation (Press et al., 1986, p77) and in particular large and inaccurate derivatives at collocation points as subsequently used by quadrature of the velocity derivative in the calculation of the transient energy. For this reason no meaningful comparison can be made with Bewley's closed-loop results.

Regarding control weightings, we set $\mathbf{R} = r^2\mathbf{I}$, thus allowing variation of control magnitude, while maintaining equivalent real and imaginary control effect on both walls.

4.2 *Optimal Estimation*

The standard LQE control problem assumes that the system has disturbance and measurement noise input processes w_d and w_n respectively

$$\begin{aligned} \dot{\mathbf{X}} &= \mathbf{AX} + \mathbf{BU} + w_d \\ \mathbf{Y} &= \mathbf{CX} + w_n \end{aligned} \tag{10}$$

and that the noise inputs are uncorrelated, zero-mean, Gaussian stochastic processes with constant power spectral density matrices $\mathbf{V}$ and $\mathbf{W}$ (Skogestad and Postlethwaite, 1996). Thus w_d and w_n are white noise processes with covariances;-

$$\mathbb{E}\left\{w_d^T w_d\right\} = \mathbf{W}\delta(t-\tau),\ \mathbb{E}\left\{w_n^T w_n\right\} = \mathbf{V}\delta(t-\tau),\ \mathbb{E}\left\{w_d^T w_n\right\} = \mathbf{0},\ \mathbb{E}\left\{w_n^T w_d\right\} = \mathbf{0} \tag{11}$$

where $\mathbb{E}$ is the expectation operator . The theory states that for an LQE state estimator

$$\dot{\hat{\mathbf{X}}} = \mathbf{A}\hat{\mathbf{X}} + \mathbf{BU} + \mathbf{L}\left(\mathbf{Y} - \mathbf{C}\hat{\mathbf{X}}\right) \tag{12}$$

where $\hat{\mathbf{X}}$ are the estimated state variables, the optimal estimator gain $\mathbf{L}$ that minimizes;-

$$\mathbb{E}\left\{\left[\hat{\mathbf{X}} - \mathbf{X}\right]^T \left[\hat{\mathbf{X}} - \mathbf{X}\right]\right\} \tag{13}$$

is given by $\mathbf{L} = \mathbf{P}\mathbf{C}^T\mathbf{V}^{-1}$ where $\mathbf{P} = \mathbf{P}^T \geq 0$ is the solution of the algebraic Riccati equation

$$\mathbf{P}\mathbf{A}^T + \mathbf{A}\mathbf{P} - \mathbf{P}\mathbf{C}^T\mathbf{V}^{-1}\mathbf{C}\mathbf{P} + \mathbf{W} = 0 \tag{14}$$

The statistical properties of the noise inputs on the present system are unknown, and so the matrices $\mathbf{V}$ and $\mathbf{W}$ can be treated as tuning parameters, in order to achieve an estimator of acceptable performance. Reasonable tuning assumptions can be made if the system state variables $\mathbf{X}$ are transformed from velocity and vorticity Chebyshev coefficients into velocity and vorticity values $\tilde{v}(y_k)$ and $\tilde{\eta}(y_k)$ respectively at the collocation points $y_k = \cos \pi k/N$

$$\mathbf{X}_{cp} = \begin{pmatrix} \tilde{v}(y_{k,k=0,2,\ldots,N-2,N}) \\ \tilde{\eta}(y_{k,k=1\ldots N-1}) \end{pmatrix} \tag{14A}$$

by means of the transformation $\mathbf{T}_{cp}$ (McKernan, 2006, p36). The system becomes;-

$$\begin{aligned} \dot{\mathbf{X}}_{cp} &= \mathbf{T}_{cp}\mathbf{A}\mathbf{T}_{cp}^{-1}\mathbf{X}_{cp} + \mathbf{T}_{cp}\mathbf{B}\mathbf{U} + w_d \\ \mathbf{Y} &= \mathbf{C}\mathbf{T}_{cp}^{-1}\mathbf{X}_{cp} + w_n \end{aligned} \tag{15}$$

Bewley and Liu (1998, p314) assumed that the process noise power spectral density $\mathbf{W}$ is a unit matrix, and estimators synthesized using this assumption will be referred to as 'uniform' estimators.

However, being in the state space of velocity and vorticity values at collocation points allows the covariance between these physically meaningful values to be set as a function of the locations of the collocation points. Here the covariance between pairs of variables is set as

$$\mathbf{W} = \begin{bmatrix} \left[(1-y_{k1}^2)(1-y_{k2}^2)\right]_{k1,k2=0,2,\ldots,N-2,N} & \mathbf{0} \\ \mathbf{0} & \left[(1-y_{k1}^2)(1-y_{k2}^2)\right]_{k1,k2=1\ldots N-1} \end{bmatrix} \tag{16}$$

where y_{k1}, y_{k2} are the locations of pairs of state variables $k1$ and $k2$ in collocation point value form $\mathbf{X}_{cp}$. This choice implies that the covariance between velocity state variables at locations y_{k1} and y_{k2} is $(1-y_{k1}^2)(1-y_{k2}^2)$, and similarly between vorticity state variables. Estimators synthesized using this assumption will henceforth be referred to as 'tuned' estimators.

For tuned estimators, when $k1 = k2$, $\mathbf{W}$ represents the variance of the noise on a single state variable, which therefore varies as $(1-y_{k1}^2)^2$. Thus disturbances on a single state variable have a higher standard deviation (the positive square root of variance) at the centreline ($y = 0$), than near the walls ($y = \pm 1$). These variances are compatible with velocity disturbances near the centreline being more variable than those near the walls and similarly for vorticity disturbances. At the walls, the velocities are set reasonably accurately by the controller, so they are given small variance (10^{-3}).

When $k1 \neq k2$, $\mathbf{W}$ represents the covariance of a pair of state variables. Pairs close to the walls have low covariances, whereas pairs close to the centreline ($y = 0$) have high covariances. Pairs where one state variable is near a wall, and the other near the centreline have covariances in between. These covariances are compatible with velocity disturbances near the centreline being physically larger than those near the walls and similarly for vorticity disturbances. The covariance between velocity and vorticity state variables is set to zero. These covariances vary smoothly over the collocation point state variables, and many other such distributions are possible e.g. those proposed by Hœpffner et al. (2005).

By the symmetry and independence of the measurements (upper and lower wall, real and imaginary

Fourier components of shear stress), it is reasonable to assume that the measurement noise covariance is $\mathbf{V} = s\mathbf{I}$, where s is a positive tuning parameter, which scales the measurement noise against the process noise.

An estimator $\mathbf{L}$ designed in terms of these velocity and vorticity state variables, may be transformed back for use on the untransformed state variables as $\mathbf{T}_{cp}^{-1}\mathbf{L}$.

4.3 *Closed-Loop LQG Output Feedback System*

The combined plant, LQR controller and LQE estimator may be combined into an LQG output feedback system, with dynamics

$$\begin{bmatrix} \dot{\mathbf{X}} \\ \dot{\hat{\mathbf{X}}} \end{bmatrix} = \begin{bmatrix} \mathbf{A} & -\mathbf{BK} \\ \mathbf{LC} & \mathbf{A} - \mathbf{BK} - \mathbf{LC} \end{bmatrix} \begin{bmatrix} \mathbf{X} \\ \hat{\mathbf{X}} \end{bmatrix} + \begin{bmatrix} \mathbf{I} & \mathbf{0} \\ \mathbf{0} & \mathbf{L} \end{bmatrix} \begin{bmatrix} \omega_d \\ \omega_n \end{bmatrix} \tag{17}$$

where the estimate and state dynamics are not independent but are intentionally coupled. If the system is recast in terms of estimator error $\mathbf{X}_{Error} = \mathbf{X} - \hat{\mathbf{X}}$ they become

$$\begin{bmatrix} \dot{\mathbf{X}} \\ \dot{\mathbf{X}} - \dot{\hat{\mathbf{X}}} \end{bmatrix} = \begin{bmatrix} \mathbf{A} - \mathbf{BK} & \mathbf{BK} \\ \mathbf{0} & \mathbf{A} - \mathbf{LC} \end{bmatrix} \begin{bmatrix} \mathbf{X} \\ \mathbf{X} - \hat{\mathbf{X}} \end{bmatrix} + \begin{bmatrix} \mathbf{I} & \mathbf{0} \\ \mathbf{I} & -\mathbf{L} \end{bmatrix} \begin{bmatrix} \omega_d \\ \omega_n \end{bmatrix} \tag{18}$$

and thus the estimator error dynamics are independent of the state dynamics, as predicted by the separation theorem (Skogestad and Postlethwaite, 1996, p353).

5 Simulations

5.1 *Initial Conditions*

Plant Worst Initial Conditions. The maximum transient energy that a stable system achieves over all time from all possible initial conditions with unit energy is here termed the *diachronic* [1] *transient energy bound*. In flow control this is a measure which is often considered in connection with non-linear effects triggering transition to turbulence. Here, the initial conditions which generate the diachronic transient energy bound are calculated, as performed by Bewley and Liu (1998) following Butler and Farrell (1992).

Following these derivations, the transient energy

$$E(t) = \mathbf{X}^T(t)\mathbf{Q}\mathbf{X}(t) \tag{19}$$

is defined as measure of how far the state is from the equilibrium point, since it considers all the state variables (in a weighted sum of squares sense). The largest possible value at time t after starting from unit initial transient energy but otherwise unknown state variables $\mathbf{X}(0)$

$$\epsilon(t) = \max_{E(0)=1} E(t) \tag{20}$$

[1] diachronic: From the Greek *dia* through, *chronos* time, from linguistics (Sykes, 1976)

is here termed the *synchronic* [2] *transient energy bound* . The diachronic transient energy bound θ is defined as the largest synchronic transient energy bound possible over all time

$$\theta = \max_{t>=0} \epsilon(t) \tag{21}$$

This may be determined as follows. If the system is diagonalizable, the state variables evolve with time t as

$$\mathbf{X}(t) = \Psi e^{\Lambda t} \chi_0 \tag{22}$$

where Λ is a diagonal matrix of the eigenvalues, Ψ is the right eigenvector matrix, and χ_0 is a vector of unknown initial modal amplitudes.

Thus

$$\epsilon(t) = \max_{\chi_0^T \Psi^T \mathbf{Q} \Psi \chi_0 = 1} \chi_0^T e^{\Lambda^T t} \Psi^T \mathbf{Q} \Psi e^{\Lambda t} \chi_0 \tag{23}$$

and $\epsilon(t)$ is given by a solution of

$$\partial / \partial \chi_0 \left(\chi_0^T e^{\Lambda^T t} \Psi^T \mathbf{Q} \Psi e^{\Lambda t} \chi_0 - \zeta \left(\mathbf{X}^T(0) \mathbf{Q} \mathbf{X}(0) - 1 \right) \right) = 0 \tag{24}$$

by the method of Lagrange multipliers, where ζ is the multiplier of the constraint equation. After differentiation by χ_0

$$\left(e^{\Lambda^T t} \Psi^T \mathbf{Q} \Psi e^{\Lambda t} \chi_0 + \left(\chi_0^T e^{\Lambda^T t} \Psi^T \mathbf{Q} \Psi e^{\Lambda t} \right)^T \right) - \zeta \left(\Psi^T \mathbf{Q} \Psi \chi_0 + \left(\chi_0^T \Psi^T \mathbf{Q} \Psi \right)^T \right) = 0 \tag{25}$$

Noting $\mathbf{Q}$ is symmetric, the final form is a generalised eigenproblem with eigenvector χ_i and eigenvalue ζ_i

$$e^{\Lambda^T t} \Psi^T \mathbf{Q} \Psi e^{\Lambda t} \chi_{0,i} = \zeta_i \Psi^T \mathbf{Q} \Psi \chi_{0,i} \tag{26}$$

Premultiplying by $\chi_{0,i}^T$, it is evident that $\epsilon(t) = \max_i \zeta_i$. The initial state variables which generate this synchronic transient energy bound are given by $\mathbf{X}_{worst} = \Psi \chi_{0,i}$.

The synchronic transient energy bound may also be cast as the square of the spectral norm of the state transition matrix e^{At}, e.g. Lim and Kim (2004) and Whidborne et al. (2004),

$$\epsilon(t) = \bar{\sigma}^2 \left(e^{At} \right) \tag{27}$$

where $A = \mathbf{Q}^{1/2} \mathbf{A} \mathbf{Q}^{-1/2}$. This form requires full matrix exponential evaluations, which, as Moler and Van Loan (2003) point out, may be unreliable, whereas in (26) Λ is diagonal, and the terms of the exponential matrix may be evaluated as scalars.

For a stable system the diachronic transient energy bound θ of $\epsilon(t)$ over all time t, can be found by a search technique. Henceforth the associated initial conditions are referred to as the "worst" initial conditions. For the open-loop system worst initial conditions, Λ and Ψ are the eigenvalues and eigenvectors of the system matrix $\mathbf{A}$. To prevent the involvement of the steady-state transpiration modes, the system matrix must be

[2] synchronic: From the Greek *syn* alike, *chronos* time, from linguistics (Sykes, 1976)

taken from a form with control by wall-normal velocity, rather than by its time derivative. For the state feedback system, Λ and Ψ are the eigenvalues and eigenvectors of the closed-loop system matrix (**A-BK**).

Estimator Energy. In a similar manner to the transient energy (19), the estimated transient energy may be defined

$$E_{Est}(t) = \hat{\mathbf{X}}^T(t)\mathbf{Q}\hat{\mathbf{X}}(t) \tag{28}$$

as measure of the energy that the estimates $\hat{\mathbf{X}}$ represent. The growth of the estimates is related to the growth of the states they attempt to reproduce (17), and this measure of estimator performance is used in the presentation of simulation results. Proximity of plant energy and estimated energy does not guarantee that their states are also close.

The error energy may be defined

$$E_{Error}(t) = \mathbf{X}_{Error}^T(t)\mathbf{Q}\mathbf{X}_{Error}(t) \tag{29}$$

as a measure of how far the estimates $\hat{\mathbf{X}}$, are from the actual state variables $\mathbf{X}$, where $\mathbf{X}_{Error} = \mathbf{X} - \hat{\mathbf{X}}$. The growth of the estimator errors $\mathbf{X}_{Error}$ and thus of E_{Error} is independent of the growth of the states the estimator attempts to reproduce (18). This measure of estimator performance is used in the tuning of estimator weights.

Estimator Zero Initial Conditions. The estimated energy bound, θ_{Est}, is defined as the largest error energy, E_{Error}, during a simulation of the system from the worst plant initial conditions $\mathbf{X}_{Worst}$, and zero estimator initial conditions, $\hat{\mathbf{X}}(0) = \mathbf{0}$, that is $\mathbf{X}_{Error}(0) = \mathbf{X}_{Worst}(0)$.

Estimator Worst Initial Conditions. The largest possible value of error energy, E_{Error}, at time t, after starting from unit initial error energy but with otherwise unknown estimator error $\mathbf{X}(0)_{Error}$, is given by the synchronic error energy bound

$$\epsilon_{Error}(t) = \max_{E_{Error}(0)=1} E_{Error}(t) \tag{30}$$

The Diachronic Error Energy Bound θ_{Error} is defined as the largest synchronic error energy bound growth possible over all time

$$\theta_{Error} = \max_{t \geq 0} \epsilon_{Error}(t) \tag{31}$$

The synchronic error energy bound may be determined from the generalised eigenproblem with eigenvector χ_i and eigenvalue ζ_i

$$e^{\Lambda^T t}\Psi^T\mathbf{Q}\Psi e^{\Lambda t}\chi_{0,i} = \zeta_i\Psi^T\mathbf{Q}\Psi\chi_{0,i} \tag{32}$$

where Ψ and Λ are the right eigenvectors and eigenvalues respectively of the estimator system matrix $\mathbf{A} - \mathbf{LC}$. The synchronic error energy bound ϵ_{Error} is $\max_i \zeta_i$ and the initial estimator errors which generate this are given by $\mathbf{X}_{Error,Worst} = \Psi\chi_{0,i}$.

The diachronic error energy bound θ_{Error} may be determined by a similar search of ϵ_{Error} over time to that used for the diachronic transient energy bound θ.

Modal and Non-Modal Components of Kinetic Energy Density in a System Transformed such that $\boldsymbol{Q} = \boldsymbol{I}$. If the state variables $\mathbf{X}$ are transformed to $\tilde{\mathbf{X}}$ such that $E(t) = \tilde{\mathbf{X}}^T\tilde{\mathbf{X}}$ then $\tilde{\mathbf{X}} = \mathbf{Q}^{1/2}\mathbf{X}$ and the state-space form (5) becomes

$$\begin{aligned}\dot{\tilde{\mathbf{X}}} &= \mathbf{Q}^{1/2}\mathbf{A}\mathbf{Q}^{-1/2}\tilde{\mathbf{X}} + \mathbf{B}\mathbf{U}\\ \mathbf{Y} &= \mathbf{C}\mathbf{Q}^{-1/2}\tilde{\mathbf{X}}\end{aligned} \tag{33}$$

Substituting the expression for the evolution of state variables (22) into the expression for perturbation energy (19) produces

$$E(t) = \tilde{\chi}_0^T e^{\Lambda^T t}\Psi^T\Psi e^{\Lambda t}\tilde{\chi}_0 \tag{34}$$

where Ψ is the matrix of right normalised eigenvectors ψ_i of $\mathbf{Q}^{1/2}\mathbf{A}\mathbf{Q}^{-1/2}$, and Λ is a diagonal matrix containing the eigenvalues λ_i, which are all assumed stable. If these eigenvectors are orthogonal, i.e. $\Psi^T\Psi = \mathbf{I}$, then

$$E(t) = \tilde{\chi}_0^T e^{(\Lambda^T+\Lambda)t}\tilde{\chi}_0 \tag{35}$$

which decays monotonically for all χ_0, as the eigenvalues Λ are stable, and thus the diachronic transient energy bound θ is unity as shown by Whidborne et al. (2004). If the eigenmodes are not orthogonal

$$\Psi^T\Psi = \begin{pmatrix} 1 & (\psi_1\cdot\psi_2) & (\psi_1\cdot\psi_3) & \dots \\ (\psi_2\cdot\psi_1) & 1 & (\psi_2\cdot\psi_3) & \dots \\ (\psi_3\cdot\psi_1) & (\psi_3\cdot\psi_2) & 1 & \dots \\ \vdots & \vdots & \vdots & \ddots \end{pmatrix} \tag{36}$$

where $(\psi_i\cdot\psi_j) = \psi_i^T\psi_j$. The energy can then be represented as per McKernan et al. (2005)

$$E(t) = \sum_{i=1}^{N} c_i^T c_i e^{(\lambda_i^T+\lambda_i)t} + \sum_{i=1}^{N}\sum_{j=1}^{N,j\neq i} c_i^T c_j(\psi_i\cdot\psi_j)e^{(\lambda_i^T+\lambda_j)t} \tag{37}$$

where $(c_0,\dots,c_N)^T = \tilde{\chi}_0$. The terms of the first summation of (37)

$$\sum_{i=1}^{N} c_i^T c_i e^{(\lambda_i^T+\lambda_i)t} \tag{38}$$

are the modal terms. They are positive for all c_i and decay monotonically, and cannot lead to any energy increase. The terms of the second summation

$$\sum_{i=1}^{N}\sum_{j=1}^{N,j\neq i} c_i^T c_j(\psi_i\cdot\psi_j)e^{(\lambda_i^T+\lambda_j)t} \tag{39}$$

are non-modal. They decay in magnitude, at different rates to the first summation, and can lead to energy increase when either

i) they are negative, that is if $c_i^T c_j(\psi_i \cdot \psi_j)$ is negative. The second term in (37) provides an upper bound $E_{pair,bound} = \max(0, -\Re(c_i^T c_j(\psi_i \cdot \psi_j)))$ on the energy growth possible from ordered mode pair i, j.

ii) they oscillate, that is if $\Im(\lambda_i^T + \lambda_j) \neq 0$. The second term in (37) provides an upper bound $E_{pair,bound} = \left|c_i^T c_j(\psi_i \cdot \psi_j)\right|$ on the energy growth possible from ordered mode pair i, j.

Of course, all dissimilar-mode pairs in the system may contribute to the aggregate energy growth, or reduce energy growth by simply decaying, as all the individual modes do, and, in the absence of repeated eigenvalues, all at different time constants.

It is noteworthy that if the system eigenvectors cannot be made accurately orthogonal by the introduction of control, selecting instead a system with the lowest dot products $(\psi_i \cdot \psi_j)$ will not necessarily lead to the lowest diachronic transient energy bound due to the presence of the other factors $c_i^T c_j$ and $e^{(\lambda_i^T + \lambda_j)t}$ in (37), and since, for the bound, c_i are selected to maximise the transient energy growth, within the overall constraint $E(0) = (c_0, \ldots, c_N)^T (c_0, \ldots, c_N) = 1$.

Differentiating (38) the modal energy growth rate terms are

$$\sum_{i=1}^{N} c_i^T c_i \left(\lambda_i^T + \lambda_i\right) e^{(\lambda_i^T + \lambda_i)t} \tag{40}$$

which have an upper bound of zero, whereas the non-modal growth rate terms are

$$\sum_{i=1}^{N} \sum_{j=1}^{N, j \neq i} c_i^T c_j(\psi_i \cdot \psi_j) \left(\lambda_i^T + \lambda_j\right) e^{(\lambda_i^T + \lambda_j)t} \tag{41}$$

which are not bounded above by zero.

Modal and Non-Modal Components of Kinetic Energy Density in a System with $Q \neq I$. If the state variables $\mathbf{X}$ are not transformed, then substituting the expression for the evolution of state variables (22) into the expression for perturbation energy (19) produces

$$E(t) = {\chi_0}^T e^{\Lambda^T t} \Psi^T \mathbf{Q} \Psi e^{\Lambda t} \chi_0 \tag{42}$$

where Ψ is the matrix of right normalised eigenvectors ψ_i of $\mathbf{A}$, and Λ is a diagonal matrix containing the eigenvalues λ_i, which are all assumed stable. The condition which guarantees modal and therefore monotonic decay is $\Psi^T \mathbf{Q} \Psi = \mathrm{diag}(d_1, \ldots, d_N), d_i > 0 \, \forall i$, since then

$$\begin{aligned} E(t) &= {\chi_0}^T e^{\Lambda^T t} \mathrm{diag}(d_1, \ldots, d_N) e^{\Lambda t} \chi_0 \\ &= \sum_{i=1}^{N} c_i^T e^{\lambda_i^T t} d_i e^{\lambda_i t} c_i \end{aligned} \tag{43}$$

which decays monotonically for all χ_0. This may be interpreted as $\Psi^T \mathbf{Q} \Psi$ not coupling any modes by being diagonal and thus preventing non-modal behaviour, and also being positive definite, and thus ensuring modal energy decay rather than growth.

5.2 *Simulations*

The state-space model is coded in Matlab^{TM}, and controllers and estimators synthesized for a range of weighting parameters. Final controllers and estimators are selected on the grounds of lowest energy bounds. Detailed linear simulations are performed for the open-loop, state feedback and output feedback systems, from the worst initial conditions, using the Matlab function `lsim`.

A finite-volume computational fluid dynamics (CFD) Navier-Stokes solver is used for the non-linear simulations. This solver makes no assumption of spectral behaviour, solves the full non-linear Navier-Stokes equations, and is completely independent of the spectral code used for the controller synthesis and linear simulations. See (McKernan, 2006) for details of the solver code, and of the modifications required, together with descriptions of the meshes, fluid properties, and boundary conditions, and of the implementation of the controller into the code.

6 Results and Discussion

This section describes the results of controller and estimator synthesis, and linear and non-linear simulations of the open-loop, state feedback and output feedback systems from the worst initial conditions. A wall-normal discretisation of $N = 100$ is used, to ensure convergence with N, except where the issue of convergence itself is investigated. As the wall-normal discretisation method is based on Chebyshev series it converges exponentially (Boyd, 2001, p46). Since the rate of convergence is so fast, successful convergence is assessed by graphical inspection.

6.1 *Controller synthesis*

LQR controllers are synthesized for a range of control weights $r = 2^1 \dots 2^{14}$, by solving the algebraic Riccati equation (ARE) (7) with $\mathbf{R} = r^2\mathbf{I}$, for discretisation $N = 100$. The Matlab Release 11 functions `care` (called via `lqr`) and `aresolv`, with both `eigen` and `schur` options are used, to investigate which performs best on such a large system. The Matlab function `aresolv` option `eigen`, produces the lowest relative residuals i.e. the Frobenius norm of the residual divided by that of the solution $\|ric(\mathbf{P})\|_F \,/\, \|\mathbf{P}\|_F$. These residuals are less than 10^{-9}, and are of acceptably small magnitude. The function reports that the problem is well posed, implying no particular problems solving the equation for such a large system, at least for this system and range of weights, although numerical problems arise outside this range. Other library routines, such as Slicot `slcares` (Benner et al., 1999; Van Huffel et al., 2004), and newer techniques, such those derived by Morris and Navasca (2005), may be able to extend the range of weights.

The variation of diachronic transient energy bound with control weight r is shown in figure 1. Several discretisations N are shown, and convergence with N is relatively fast and has occurred by $N = 30$. The continued convergence at high N again demonstrates the existence of few problems solving this particular system when N **is** very large. The range of weights is appropriate for controller synthesis, since it covers convergence at low r, where the control effort is large and the energy is small. As the control weight rises, the control effort falls, and thus the energy bound rises. The variation here is monotonic, but need not be if very high control (very low weight) itself increases transient energy, as investigated by McKernan et al. (2005). A value of $r = 128$ was selected for subsequent simulations, as this produces almost the lowest diachronic transient energy bound, without being unnecessarily small, which would lead to unnecessarily large control effort. Low diachronic transient energy bound implies low transient energy over all unit

energy initial conditions and all time, thus reducing the possibility of non-linear behaviour and transition to turbulence.

6.2 *Estimator synthesis*

LQE estimators are synthesized for a range of measurement noise weights s, by solving the algebraic Riccati equation (ARE) (14) with $\mathbf{V} = s\mathbf{I}$, using the Matlab functions `care` (called via `lqe`) and `aresolv`, with both `eigen` and `schur` options, for $N = 100$. The Matlab function `aresolv` option `eigen` generally produces the lowest relative residuals, less than 10^{-7} for the tuned estimator, and the function reports that the problem is well posed. The residuals are of acceptably small magnitude, but not as small as those found during the synthesis of controllers.

Good estimator performance requires that the estimator poles be faster (real part more negative) than the plant poles. However, the current plant has a large number of poles, the faster ones of which are not known accurately, and it is not feasible to make the slowest estimator poles faster than these.

Convergence of Estimated Energy Bound θ_{Est} with N is relatively slow, as compared to that of the controller, and does not occur until $N = 70$, which is consistent with the behaviour of the wall eigenvector gradients used for observation as found by McKernan (2006).

The worst estimator initial error conditions $\mathbf{X}_{Error,Worst}$ are found to be very exacting, since they lead to growth of diachronic error energy bound θ_{Error} of comparable magnitude to the plant diachronic transient energy bound. Since the estimators are stable and their states converge upon the plant states, it is difficult to see how such estimator initial conditions could occur. In contrast, zero estimates $\hat{\mathbf{X}} = \mathbf{0}$ are to be expected upon initialisation of the estimators, implying initial errors equal to the plant initial conditions, $\mathbf{X}_{Error} = \mathbf{X}_{Worst}$.

Furthermore, for the LQG controller, both plant and estimator initial conditions need to be selected. It is not clear how to select the relative magnitudes of the initial plant energy and estimator error energy, since the plant energy is a physical quantity which leads to transition, whereas the estimator error energy is not. Again, zero initial estimates are a reasonable assumption to make.

Accordingly, zero initial estimates are selected in preference to the worst estimator initial error conditions for further simulations in the present work. Plots of estimated energy bound and slowest estimator pole (McKernan, 2006) favour the use of the tuned estimator over the uniform estimator, at low measurement noise. A weight of $s = 2^{-6} \approx 0.0156$ is selected for further work, as this produces close to the lowest estimated energy bound.

6.3 *Initial Conditions*

Synchronic Transient Energy Bound ϵ vs Time. Figure 2 shows open-loop synchronic transient energy bound, $\epsilon(t)$, against time. As the eigenvalues in the test case are real and stable, the only mechanism for growth is non-modal, and this is confirmed by the non-linear nature of the logarithmic plot. The graph of the synchronic transient energy bound against time is convex, and so there are no root bracketing problems. A golden section search (Press et al., 1986, p277) produces a maximum at 4896.94 at $t = 379.16$ and thus $\theta = 4896.94$. This value compares well with $\theta = 4897$ at $t = 379$ as reported by Butler and Farrell (1992, p1647). A bisection search (Press et al., 1986, p246) based on the criteria $\mathbf{X}^T\mathbf{A}\mathbf{X} = 0$, as described by Whidborne et al. (2004) proves inaccurate in this case.

As shown from (27), the synchronic transient energy bound can be expressed as the square of the spectral

norm of the state transition matrix. Now the Frobenius norm squared provides a upper bound on the square of the spectral norm, and $1/\min(l,m)$ times the Frobenius norm squared provides a lower bound, where the matrices are l by m (Skogestad and Postlethwaite, 1996, p520). Figure 2 also shows the Frobenius norm of the state transition matrix and it can be seen that the synchronic transient energy bound $\epsilon(t)$ lies within the correct bounds. The corresponding plots for the LQR controlled systems are qualitatively similar to figure 2.

Investigation of Open-Loop and Closed-Loop Diachronic Transient Energy Bound θ. Investigations of the modes which lead to maximum open-loop diachronic transient energy bound are performed. For the remainder of this subsection, the state variables employed are transformed to $\tilde{\mathbf{X}}$, as defined in section 5.1 such that $E = \tilde{\mathbf{X}}\tilde{\mathbf{X}}$, and the eigenvectors are expressed in the same state variables, and normalised to unit magnitude, unless stated otherwise. Eigenvectors are in order of increasing eigenvalue stability.

Figure 3 shows a bar chart of the dot product between pairs of modes from 1 to 25. The main diagonal has unit magnitude, due to the normalisation chosen. The next highest dot products are on the adjacent diagonals, corresponding to mode pairs comprising consecutive mode pairs. The dot products of consecutive open-loop $\tilde{\mathbf{X}}$ modes, together with the vorticity $\tilde{\eta}$ eigenvectors (the velocity eigenvectors are much smaller in magnitude) appear in figure 4. It can be seen that a high dot product corresponds to vorticity eigenvectors of similar shape (within reflection), which is to be expected since similar mode shapes imply similar state variable vectors, and thus high dot products.

Figure 5 shows the same plot for the LQR system, for which the diachronic transient energy bound is reduced. It can be seen that in general the modes have comparable dot-products as in the open-loop figure 4 and thus remain as non-normal or non-orthogonal as in the open-loop case. The diachronic transient energy bound is known to be minimised to a value of unity when the modes are made precisely orthogonal but when precise orthogonality is not achieved, as here, the effect of increasing orthogonality may not produce the lowest energy, as shown in section 5.1, and thus the absence of a distinct reduction of non-normality is not surprising. It is suggested that the LQR controller directly affecting the modal orthogonality is unlikely, contrary to observations by Bewley and Liu (1998, p343).

The open-loop upper bounds on mode pair energy growth $E_{pair,bound}$, calculated using the expressions derived in section 5.1, from the worst initial conditions, are presented in figure 6. As would be expected, the chart is symmetrical. Few mode pairs appear to have a significant potential for transient energy growth, with the exception of pair 4,5.

Figure 7 shows the upper bounds on mode pair energy growth after the application of LQR control, from the worst initial conditions. More mode pairs have a significant potential for transient energy growth, those with the largest potential being 1,5 and 1,4. These significant pairs are not consecutive modes, unlike the open loop significant pair 4,5. The largest upper bound of all the pairs has fallen from approximately 2.5×10^5 to 3×10^3, due to the application of LQR control.

6.4 *Linear Simulations*

The results of linear simulations on the open- and closed-loop systems are investigated in detail in this section.

Open-Loop Linear Simulation. Five different plant discretisations, $N = 10, 20, 30, 40, 50$, are simulated and the results are presented in figure 8, of open-loop transient energy against time. The results are

converged at $N = 20$ and above, showing that a low discretisation of $N = 20$ is adequate to simulate the open-loop case. Since the diachronic transient energy bound is maximised over time, and larger than one, the transient energy starts at a minimum. Here the transient energy reaches the diachronic transient energy bound value of 4896.94 at time 379.5, close to the predicted value of 4896.94 at time 379.16 from section 6.3, before decaying to zero. The small discrepancy is caused by the linear simulation results being provided at discrete timesteps. Calculations using (37) show that mode pair $(4, 5)$ provides substantial growth of transient energy as predicted in figure 6 (McKernan, 2006, p151).

LQR State Feedback Linear Simulation. As the $\tilde{v}$ initial conditions are symmetrical about the centreline, the control signal at the lower wall $\dot{\tilde{v}}(y = -1)$ is identical to that at the upper wall. However, as the sense of the upper and lower wall boundaries are reversed, transpiration suction at the upper wall, $\tilde{v}(y = 1) > 0$, corresponds to blowing at the lower wall. Figure 9 shows the LQR control signal at the upper wall $\dot{\tilde{v}}(y = 1)$ against time.

Figure 10 displays the time integral of the LQR control signal at the upper wall, namely the Fourier coefficient of the upper wall velocity, which has real and imaginary components to allow variations in both the magnitude and spatial phase of the transpiration. For the test case considered here, the upper wall transpiration velocity is imaginary, i.e. in phase with the disturbance velocity but out of phase with the vorticity which is assumed real (McKernan, 2006, p43). The coefficient magnitude peaks at approximately 1.75, i.e. 1.75 times the base flow centreline velocity. However, this figure is for a unit initial transient energy. The kinetic energy density of the base flow is $1/15 \approx 0.0667$. For an initial perturbation energy of 10% of the base flow energy, the upper wall velocity would peak at around $1.75 \times \sqrt{0.00667}$, approximately 0.14, and for a perturbation energy of 1% of base flow, the velocity would peak at approximately 0.045 times the base flow centreline velocity. This represents the transpiration at reasonable velocity.

The double time integral of the LQR control signal at the upper wall, namely the Fourier coefficient of the upper wall fluid quantity transpired, versus time is displayed in figure 11. Although the net amount of fluid transpired is zero since the distribution is sinusoidal, this coefficient represents the magnitude of the sinusoidal distribution. The coefficient magnitude peaks at around 515, i.e. 515 times the channel half height, for a unit energy initial perturbation. For an initial perturbation energy 1% of that of the base flow, the quantity would peak at approximately 13.3 times the channel half height. This represents the transpiration of a comparatively large amount of fluid, requiring a large associated reservoir or distribution system. The final coefficient is not zero, representing a permanent transport of transpiration fluid within each spatial period, and thus any reservoirs do not return to their initial level, but instead fluid has been permanently moved between them.

Figure 12 presents the LQR transient energy against time. The controller is able to limit the transient energy to 848.80, which is consistent with the value of 848.81 from figure 1, as compared to the open-loop value of 4896.94. Thus the controller effectively limits the growth of the worst case disturbance. Three different discretisations N are shown, and convergence has occurred for even the lowest $N = 30$.

The LQR controller minimises the *time integral* of the transient energy plus weighted control effort, from all initial conditions, rather than the diachronic transient energy bound itself, although the diachronic transient energy bound has been reduced from 4896.94 to 848.80 as a consequence. Calculations using (37) show that mode pairs $(1, 4)$ and $(1, 5)$ provide substantial growth of transient energy as predicted in figure 6 (McKernan, 2006, p158).

Open-Loop LQE State Estimation Linear Simulation. LQE estimated transient energy against time is presented in figure 13. The tuned estimator converges on the plant energy much faster than the uniform estimator. Figure 14 shows LQE transient energy against time, for the tuned estimator, for several discretisations N. It is evident that the behaviour of the estimator is not fully converged below approximately $N = 50$.

LQG Output Feedback Linear Simulation. Figure 15 shows the LQG transient energy and estimated transient energy against time. The controller is able to produce an diachronic transient energy bound of approximately 934.00, only slightly larger than the LQR state feedback value of 848.80.

6.5 *Summary of Diachronic Transient Energy Bound θ Results*

As a check, table 1 exhibits a summary of the diachronic transient energy bound values of the open-loop and LQR state feedback systems, from both the diachronic transient energy bound eigensystem (26), and the linear simulation from the worst initial conditions. The small discrepancies are thought to be due to numerical inaccuracies, amongst which are the discrete time steps used in the linear simulations.

Table 2 shows a summary of the diachronic transient energy bound values from the open-loop and feedback systems, and also includes the estimated energy bound achieved by the LQE estimator on the open-loop and LQG systems, from zero initial estimates.

6.6 *Choice of Discretisation N for Controller in Non-Linear Simulations*

The non-linear simulations require significantly more computing time than the linear ones, in the order of days rather than minutes, on a Pentium 4^{TM} personal computer. It is appropriate to consider the choice of discretisation for the controllers to be applied to the non-linear models. Since no controller reduction is employed, this equates to the discretisation of the spectral model used for the controller synthesis. The issue of discretisation of the non-linear model itself is considered by McKernan (2006).

For the LQR controller synthesis to converge $N = 30$ is sufficient (section 6.1), and for the LQE estimator synthesis $N = 70$ is sufficient (section 6.2). The linear simulations require $N = 30$ for the LQR system and $N = 50$ for the LQE system (section 6.4). The more exacting requirement of LQE is thought to be related to the convergence of the wall gradients and observability.

For the observability and wall gradients to have converged for the first 20 modes, approximately $N = 100$ is required according to McKernan (2006). The need for fine discretisation at the wall is well known within the fluid dynamics community. Accordingly, controllers synthesized using a spectral model using $N = 100$ are used within the non-linear simulations.

6.7 *Non Linear Simulations*

A linear controller synthesized using a linearisation of a non-linear model will be able to stabilise the full model given initial conditions near the linearisation equilibrium point, and provided the trajectories do not stray far from the equilibrium point. However, if large transients take trajectories far away from the equilibrium point, non-linear effects may predominate and the system may not be stable.

This section explores the performance of the controllers on a non-linear model of the plant, from small and large initial perturbations. The non-linear simulations presented here cannot become fully turbulent

as they are not three-dimensional, but they are capable of accurately modeling the initial evolution of instabilities.

Small Perturbation Results. For the small perturbation simulations, the open-loop initial maximum $\tilde{v}$ is $10^{-4}U_{cl}$. This value corresponds to an initial transient energy of E_0 (2.26×10^{-9}), and has been shown by McKernan (2006, p166) to induce less than 1% non-linearity (as defined by the ratio of non-linear convection $(\vec{u} \cdot \nabla)\,\vec{u}$ to base flow convection $\left(\vec{U}_b \cdot \nabla\right)\vec{u}$ in the Navier-Stokes equations (3)) in a region that covers more than 90% of the flow field area. Closed-loop worst initial conditions of equal transient energy to the corresponding open-loop case are used.

Results from non-linear finite-volume CFD simulations from small perturbation initial conditions are generally close to those from the spectral linear simulations, despite the fact that the finite-volume and spectral simulation codes have been independently developed. The only exception is the behaviour of the estimator in the LQG output feedback simulations, which shows a small discrepancy, although the plant energies agree well.

These small perturbation non-linear simulations show agreement between peak transient energy as computed from the states by $E = \mathbf{X}^T\mathbf{Q}\mathbf{X}$ and as calculated by direct integration over the mesh using (9) to within 0.3% for the LQR system. This result shows that the calculation of the states is substantially correct, and also that the energy matrix $\mathbf{Q}$ is correctly formulated.

Large Perturbation Results. For the large perturbation simulations, the initial transient energy is $10^4 E_0$, corresponding to an open-loop initial maximum $\tilde{v}$ of approximately $10^{-2}U_{cl}$.

Open-Loop Non-Linear Simulation. The open-loop transient energy time history, from this larger initial perturbation, for both linear and non-linear simulations, is displayed in figure 16. The linear and non-linear simulations agree initially for a period of non-normal growth up to time approximately 50 units. Thereafter the linear simulation increases to complete the non-normal growth to transient energy of 0.111, corresponding to an diachronic transient energy bound of 4896.94, and thence continue with decay, but the non-linear simulation reaches a saturated state with peak transient energy of 0.0240 at time approximately 124.5 units, and thereafter decays. The decay continues beyond $t = 1500$ (not shown), at approximately the same rate as at $t = 1000$. Although non-linear simulation soon deviates from the linear results, the earliest growth appears to be at a rate identical to that of the linear system non-modal phase.

Regarding estimation, figure 16 also shows the open-loop estimated transient energy against time. In this case, the performance of the linear estimator on the non-linear plant model is poor, as it overshoots the plant energy.

LQR State Feedback Non-Linear Simulation. Figure 17 presents the closed-loop LQR transient energy versus time, from this larger initial perturbation, for both linear and non-linear simulations. The controller reduces the transient energy, and the difference between the linear and non-linear simulation is somewhat reduced, as compared to the open-loop case. The controller has reduced the open-loop non-linear peak transient energy from 0.024 to 0.0093, a reduction of approximately 61% which is not nearly such a great reduction as that in linear simulation where the diachronic transient energy bound falls approximately 83%. The peak nonlinear LQR transient energy of 0.0093 is approximately half the linear value of 0.019. The controller is acheiving a lower energy density on the non-linear simulation, as energy levels are in general lower in the non-linear simulation. The wall transpiration velocities required in the non-linear simulation are comparable with those in the linear one.

The large perturbation CFD simulation for the LQR system showed poor agreement between the peak transient energy as computed from the states using $\mathbf{X}^T\mathbf{Q}\mathbf{X}$ from (19) and as calculated by direct integration over the mesh using (9). The peak transient energy as computed from the states under estimates that from direct integration by 44%. This is thought to be due to disturbances at wave number pairs other than α, β being present at peak E in the non-linear magnitude CFD simulation.

LQG Output Feedback Non-Linear Simulation. Figure 18 shows the LQG transient energy versus time. The linear controller is unable to stabilize the non-linear plant model at this level of initial disturbance. Since the LQR controller is able to stabilise the test case at this energy level, the deficiency appears to be in the estimator, and indeed its behaviour is poor, as its estimated energy overshoots the plant energy around time 120, and diverges erratically from time 720 onwards. Since an implicit method is employed, to avoid stiffness problems, the estimator integration scheme is guaranteed to be stable, and thus integration instability is not the cause of this erratic behaviour.

Results from a smaller initial disturbance corresponding to an open-loop worst initial condition with $v_{max} = 7.5 \times 10^{-3} U_{cl}$, i.e. energy of $5625 E_0$ are presented in figure 19. The linear controller is able to stabilize the non-linear plant model at this smaller level of initial disturbance, approximately half that of the level which could not be stabilised. This time the estimated energy overshoots but does not diverge. The transient energy is limited to 0.01, as compared to the open-loop plant which reaches approximately 0.04 (not shown).

6.8 *Summary of Simulation Results*

Table 3 show a summary of the linear and non-linear simulation results. At the perturbation sizes used here, non-linear effects reduce the energy of large perturbation simulations below the level of scaled small perturbation results, with the exception the LQG unstable large perturbation simulation.

7 Conclusions

This paper has described the synthesis and validation of output and state feedback optimal controllers for plane Poiseuille flow, and has investigated aspects of the transient energy growth of the controlled and uncontrolled systems.

Tuned process noise weights for the optimal estimator were chosen to reflect the possible size variations in disturbances across the channel, as an alternative to uniform weights and proved better at following the plant worst case initial conditions from zero initial estimates. Estimation required finer model wall-normal discretisation than state feedback control required.

Regarding feedback control, although the sinusoidal transpiration was guaranteed to have a zero net flux over whole streamwise or spanwise periods, and thus also over any time span, its magnitude was such that at any particular point the transpiration of comparatively large quantities of fluid were required. Controller implementation schemes mooted e.g. by (Ho and Tai, 1998) envisage the use of microelectrical machines (MEMs) based on small reservoirs, but these schemes would appear unable to provide the quantities of fluid required for optimal control of the test case based on early transition considered here.

Non-linear simulations on linear sized perturbations reproduced the linear simulation results . The overall agreement between the linear spectral results and the independent finite volume results at low

levels of disturbance provides good evidence that both are correct under these conditions. A non-linear simulation of the open-loop plant from a large (non-linear sized, $v_{max} = 10^{-2}U_{cl}$) worst initial perturbation showed that the flow saturates but appears stable. Although the simulation soon deviates from the linear results, initially they both grow at the non-normal rate of the linear simulations.

A non-linear simulation of the plant with LQR state feedback from a large worst initial perturbation again saturates but remain stable. The state feedback reduces the peak transient energy below open-loop values. Thus the linear and non-linear results are closer than the open-loop results. The LQG controller is unable to stabilise the non-linear plant at this level of initial perturbation. The estimator initially behaves well, but overshoots and diverges, leading the controller to destabilise the plant. From an initial perturbation of half this energy level, the estimator energy again overshoots the plant, but it does not diverge, and the controlled plant keeps the transient energy well below the open-loop value.

This study has not investigated the effects of uncertainty such as modelling errors, plant disturbances and measurement noise, on closed-loop performance. Although LQG control contains a specific model for disturbances and noise, this model does not adequately address their uncertainty (Zhou et al., 1996, p214). Further study would require investigation of controller robustness to modelling uncertainty as performed by Bewley and Liu (1998) and Baramov et al. (2004).

References

Balogh, A., Liu, W-J. and Krstic, M.: 2000, Stability enhancement by boundary control in 2D channel flow - Part II: Numerical implementation and stability, *Proc. 2000 American Control Conference (ACC 2000), Jun 28-30, 2000*, Chicago, Illinois, pp. 4259–4263.

Baramov, L., Tutty, O.R. and Rogers, E.: 2001, H-infinity control for non-periodic planar channel flows, *Proc. 40th IEEE Conference on Decision and Control, Dec 04-07, 2001*, Orlando, Florida, pp. 4950–4955.

Baramov, L., Tutty, O.R. and Rogers, E.: 2004, H-infinity control of nonperiodic two-dimensional channel flow, *IEEE Trans. Control Syst. Technol.* **12**(1), 111–122.

Benner, P., Mehrmann, V., Sima, V., Van Huffel, S. and Varga, A: 1999, SLICOT — A subroutine library in systems and control theory, *in* B.N. Datta (ed.), *Applied and Computational Control, Signals, and Circuits*, Vol. 1, chapter 10, Birkhauser, Boston, pp. 499–539.

Bewley, T.R. and Liu, S.: 1998, Optimal and robust control and estimation of linear paths to transition, *J. Fluid Mech.* **365**, 305–349.

Bewley, T.R., Moin, P. and Temam, R.: 2001, DNS-based predictive control of turbulence: An optimal benchmark for feedback algorithms, *J. Fluid Mech.* **447**, 179–225.

Boyd, J.P.: 2001, *Chebyshev and Fourier Spectral Methods*, second edn, Dover, Mineola,New York.

Butler, K.M. and Farrell, B.F.: 1992, Three-dimensional optimal perturbations in viscous shear flow, *Phys. Fluids* **4**(8), 1637–1650.

Carlson, D.R., Widnall, S.E. and Peeters, M.F.: 1982, A flow-visualization study of transition in plane Poiseuille flow, *J. Fluid Mech.* **121**, 487–505.

Hinrichsen, D. and Pritchard, A.J.: 2005, *Mathematical Systems Theory I: Modelling, State Space Analysis, Stability and Robustness*, Springer-Verlag, Berlin.

Hinrichsen, D., Plischke, E. and Wirth, F.: 2002, State feedback stabilization with guaranteed transient bounds, *Int. Symp. Math. Theory Networks & Syst.*, South Bend, Indiana, pp. CDROM – paper 2132.

Ho, C.M. and Tai, Y.C.: 1998, Micro-electro-mechanical-systems (mems) and fluid flows, *Annu. Rev. Fluid*

Mech. **30**, 579–612.

Hœpffner, J., Chevalier, M., Bewley, T.R. and Henningson, D.S.: 2005, State estimation in wall-bounded flow systems. Part 1. Perturbed laminar flows, *J. Fluid Mech.* **534**, 263–294.

Joshi, S.S., Speyer, J.L. and Kim, J.: 1999, Finite dimensional optimal control of Poiseuille flow, *J. Guid. Control Dyn.* **22**(2), 340–348.

Lauga, E. and Bewley, T.R.: 2004, Performance of a linear robust control strategy on a nonlinear model of spatially developing flows, *J. Fluid Mech.* **512**, 343–374.

Lim, J. and Kim, J.: 2004, A singular value analysis of boundary layer control, *Phys. Fluids* **16**(6), 1980–1988.

McKernan, J.: 2006, *Control of Plane Poiseuille Flow: A Theoretical and Computational Investigation*, PhD thesis, Department of Aerospace Sciences, School of Engineering, Cranfield University.

McKernan, J., Whidborne, J.F. and Papadakis, G.: 2005, Minimisation of transient perturbation growth in linearised Lorenz equations, *Proc. 16th IFAC World Congress July 4-8, 2005*, Prague.

Moler, C. and Van Loan, C.: 2003, Nineteen dubious ways to compute the exponential of a matrix, twenty-five years later, *SIAM Rev.* **45**(1), 3–49.

Morris, K.A. and Navasca, C.: 2005, Solution of algebraic Riccati equations arising in control of partial differential equations, *in* J. Cagnol and J.P. Zolesio (eds), *Control and Boundary Analysis*, Vol. 240 of *Lecture Notes in Pure and Applied Mathematics*, CRC Press, Boca Raton, Fl, pp. 257–280.

Orszag, S.A.: 1971, Accurate solution of the Orr-Sommerfeld stability equation, *J. Fluid Mech.* **50**(4), 689–703.

Press, W.H., Flannery, B.P., Teukolsky, S.A. and Vetterling, W.T.: 1986, *Numerical Recipes*, CUP, Cambridge.

Skogestad, S. and Postlethwaite, I.: 1996, *Multivariable Feedback Control*, Wiley, Chichester, England.

Sykes, J.B. (ed.): 1976, *The Concise Oxford Dictionary*, 6th edn, OUP, Oxford.

Trefethen, L.N., Trefethen, A.E., Reddy, S.C. and Driscoll, T.A.: 1993, Hydrodynamic stability without eigenvalues, *Science* **261**, 578–584.

Van Huffel, S., Sima, V., Varga, A, Hammarling, S. and Delebecque, F.: 2004, High-performance numerical software for control, *IEEE Control Syst. Mag.* **24**(1), 60–76.

Whidborne, J.F., McKernan, J. and Papadakis, G.: 2004, Minimization of maximum transient energy growth, *Proc. UKACC Control 2004 Sep 06-09, 2004*, Bath, UK.

Whidborne, J.F., McKernan, J. and Steer, A.J.: 2005, On minimizing maximum transient energy growth, *COA Report No. 0501*, Department of Aerospace Sciences, School of Engineering, Cranfield University.

Yeoh, S.L., Papadakis, G. and Yianneskis, M.: 2004, Large eddy simulation of turbulent flow in a Rushton impeller stirred reactor with sliding-deforming mesh methodology, *Chemical Engineering Technology* **27**(3), 257–263.

Zhou, K., Doyle, J.C. and Glover, G.: 1996, *Robust and Optimal Control*, Prentice-Hall, Upper Saddle River, NJ.

Table 1. Open-Loop and LQR Diachronic Transient Energy Bound θ by Eigensystem Calculation (26) and Linear Simulation

Eigensystem Calculation (26)				Linear Simulation			
OL	Time	LQR	Time	OL	Time	LQR	Time
4896.94	379.16	848.81	187.03	4896.94	379.5	848.80	187.5

Table 2. Diachronic Transient Energy Bound θ for All Open- and Closed-Loop Systems, by Linear Simulation

OL θ	LQR θ	OL LQE θ_{Est}	LQG θ	LQE θ_{Est} in LQG
4896.94	848.80	4235.73	937.00	729.30

Table 3. Transient Energy E from Non-linear Simulations from Small and Large Initial Disturbances (* indicates unstable.)

System	$\max_y \tilde{v}(t=0)$	$E(t=0)$	$\max_{t<600} E$	$\max_{t<600} E_{est}$
OL/ LQE	10^{-4}	E_0	$1.10 \times 10^{-5} @ t = 378.6$	$9.16 \times 10^{-6} @ t = 383.2$
	7.5×10^{-3}	$5625 E_0$	$1.20 \times 10^{-2} @ t = 161.2$	$3.15 \times 10^{-2} @ t = 204.9$
	10^{-2}	$10^4 E_0$	$2.40 \times 10^{-2} @ t = 124.5$	$4.77 \times 10^{-2} @ t = 170.4$
LQR		E_0	$1.90 \times 10^{-6} @ t = 187.0$	-
		$10^4 E_0$	$9.51 \times 10^{-3} @ t = 89.7$	-
LQG		E_0	$2.12 \times 10^{-6} @ t = 196.3$	$1.79 \times 10^{-6} @ t = 227.7$
		$5625 E_0$	$7.49 \times 10^{-3} @ t = 173.8$	$9.96 \times 10^{-3} @ t = 238.2$
		$10^4 E_0$	$3.12 \times 10^{-2} @ t = 600^*$	$2.30 \times 10^{-2} @ t = 481.3$

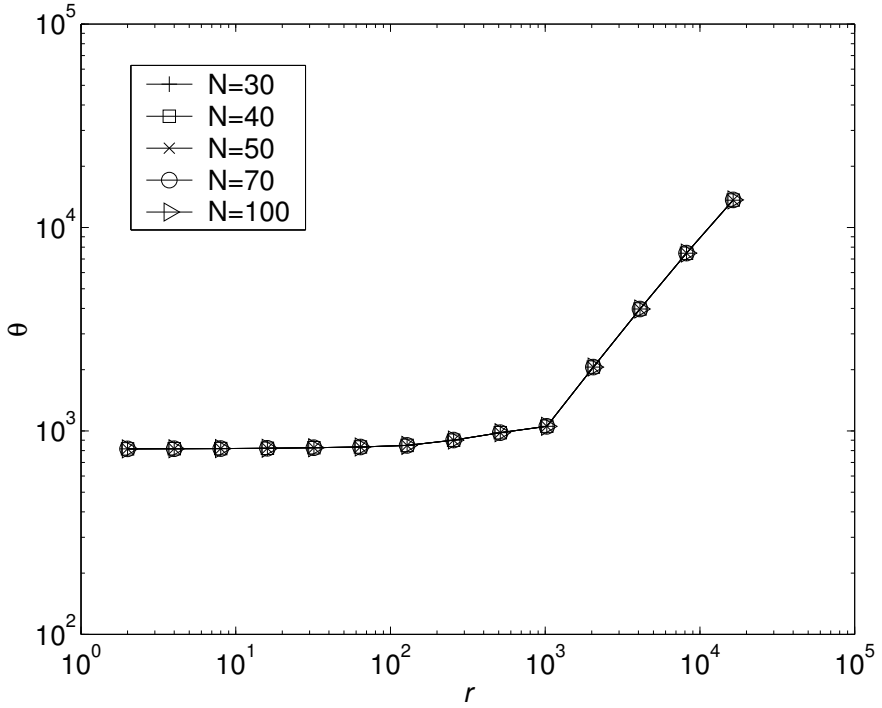

Figure 1. LQR Diachronic Transient Energy Bound θ vs Control Weight r, for Different Discretisations N

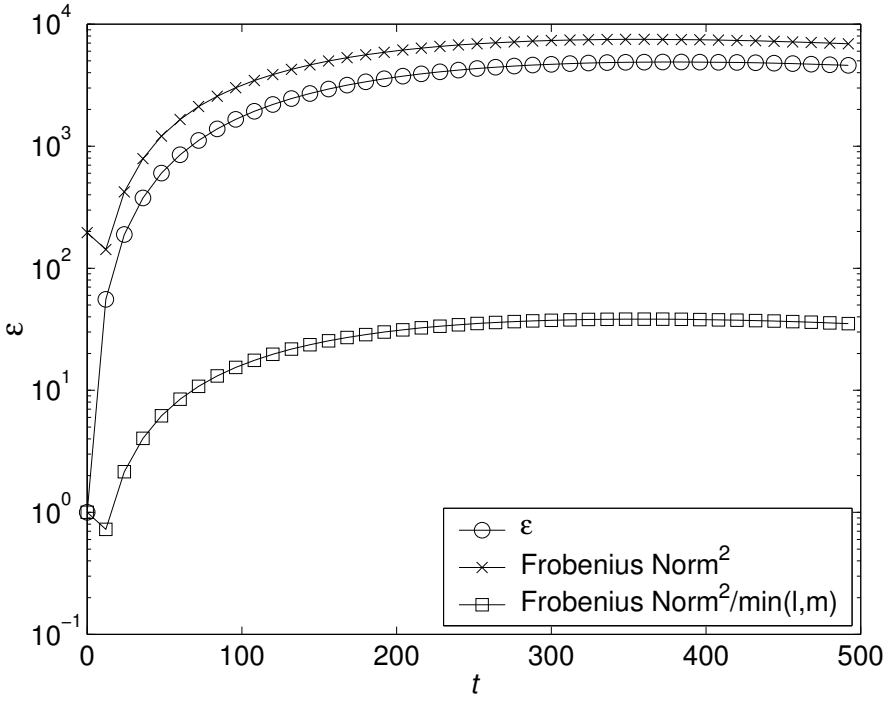

Figure 2. Open-Loop Synchronic Transient Energy Bound ϵ vs t, $N = 100$

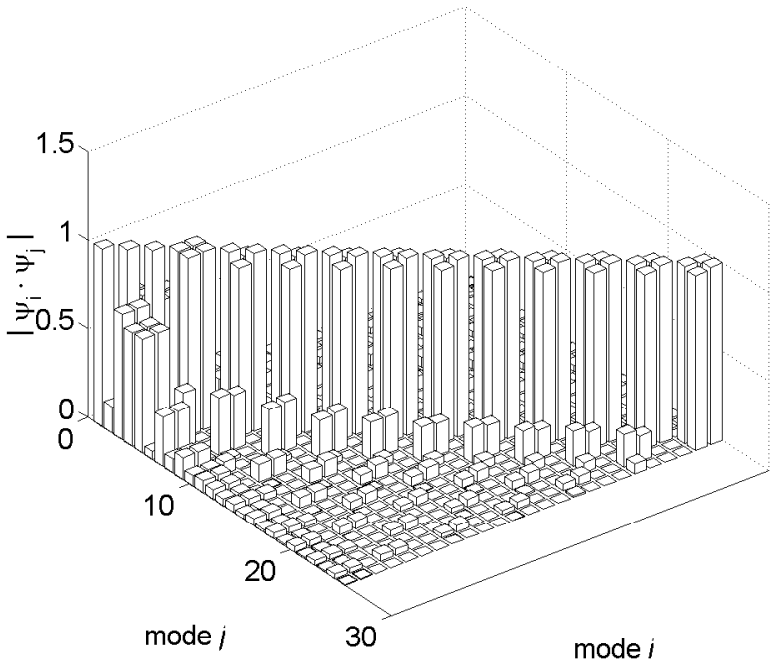

Figure 3. Open-Loop Bar Chart of Mode Pair Dot Products, $N = 100$

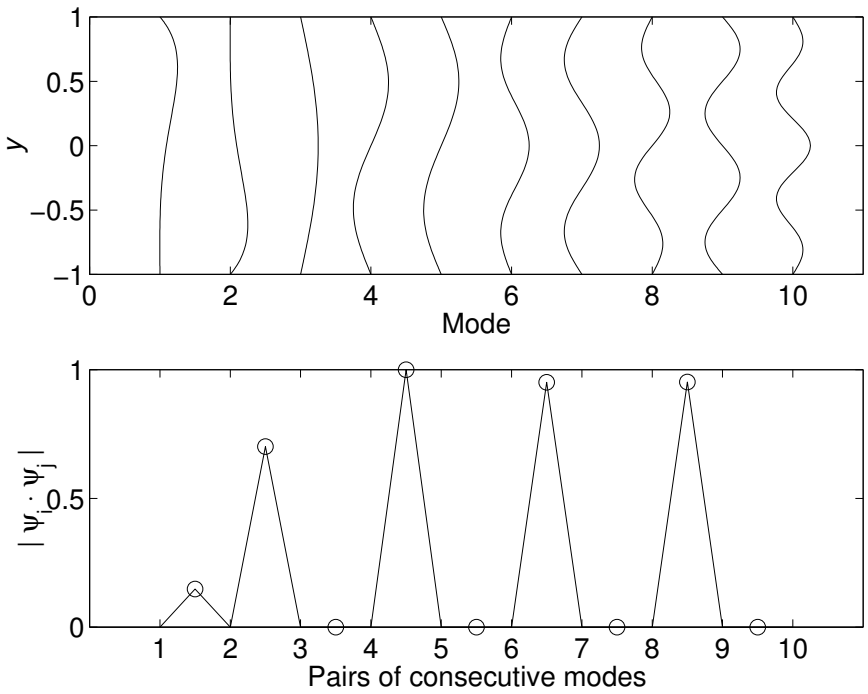

Figure 4. Open-Loop: Upper Plot - Vorticity Eigenvectors, Lower Plot - Dot Product of Consecutive $\tilde{\mathbf{X}}$ Eigenvectors, $N = 100$

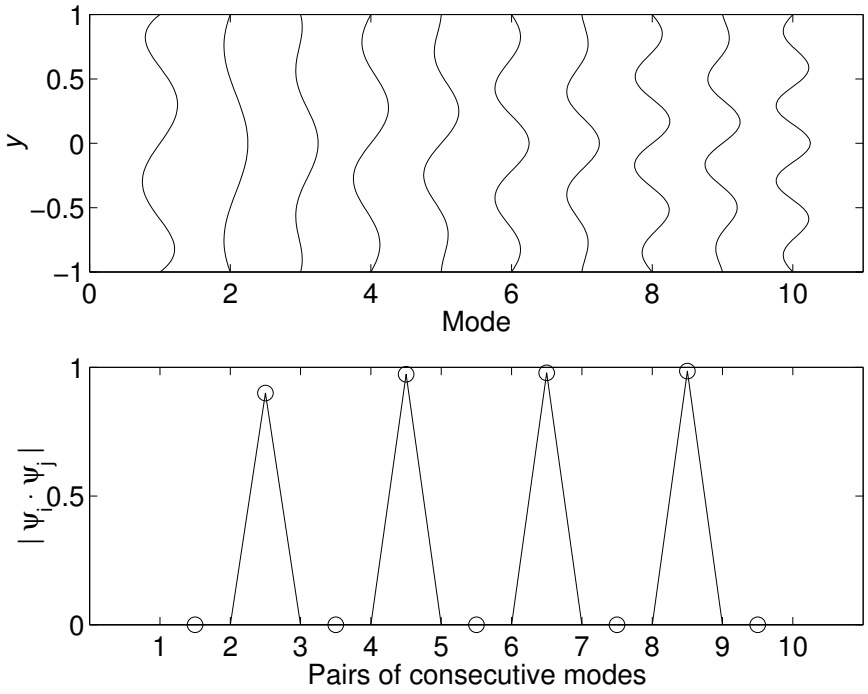

Figure 5. LQR: Upper Plot - Vorticity Eigenvectors, Lower Plot - Dot Product of Consecutive $\tilde{\mathbf{X}}$ Eigenvectors, $N = 100$

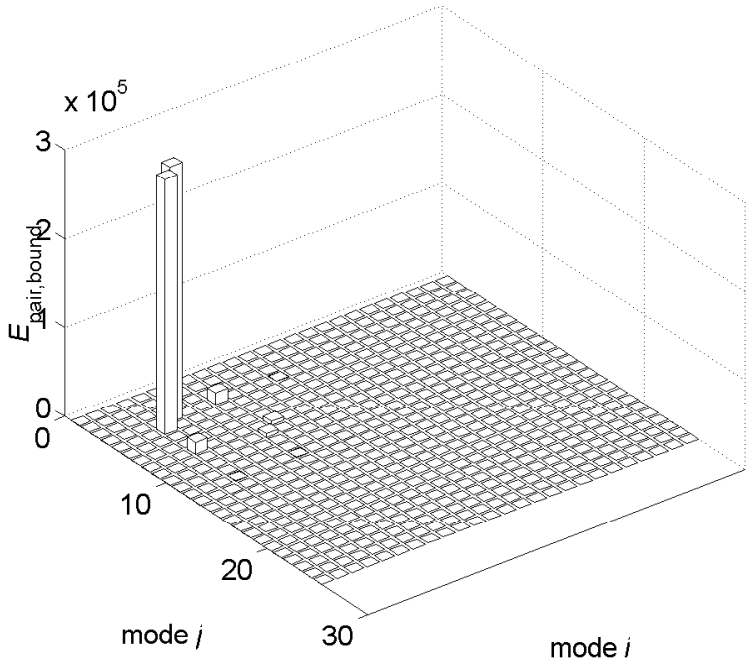

Figure 6. Open-Loop Upper Bound on Mode Pair Energy Growth $E_{pair,bound}$, $N = 100$

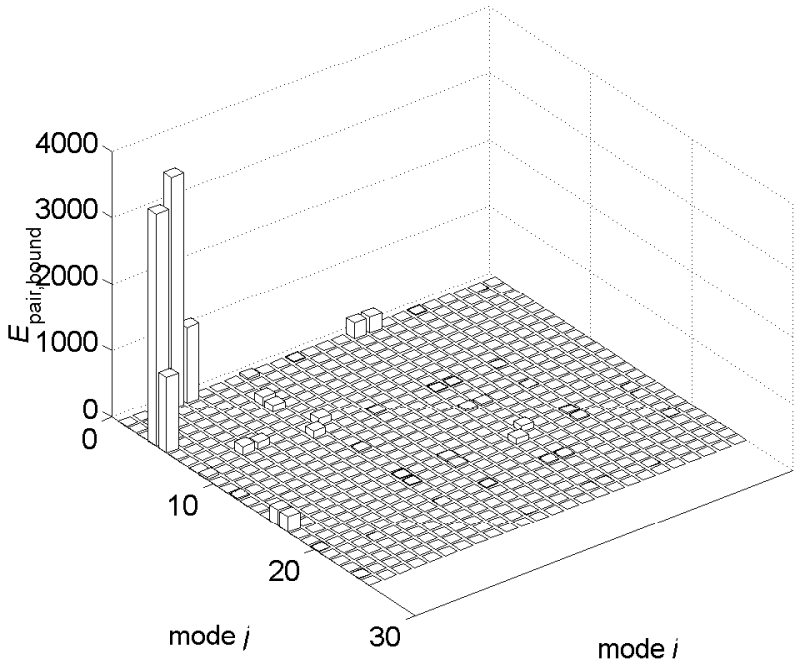

Figure 7. LQR Upper Bound on Mode Pair Energy Growth $E_{pair,bound}$, $N = 100$

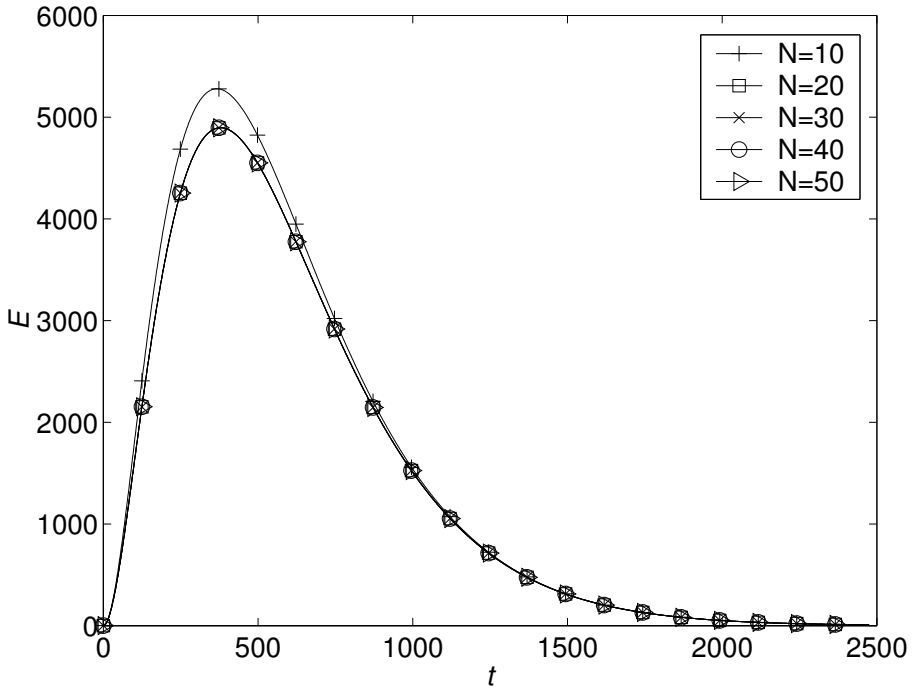

Figure 8. Open-Loop Transient Energy E vs t, for Various Discretisations N, from initial conditions $\mathbf{X}_{worst}$ scaled to $E = 1$

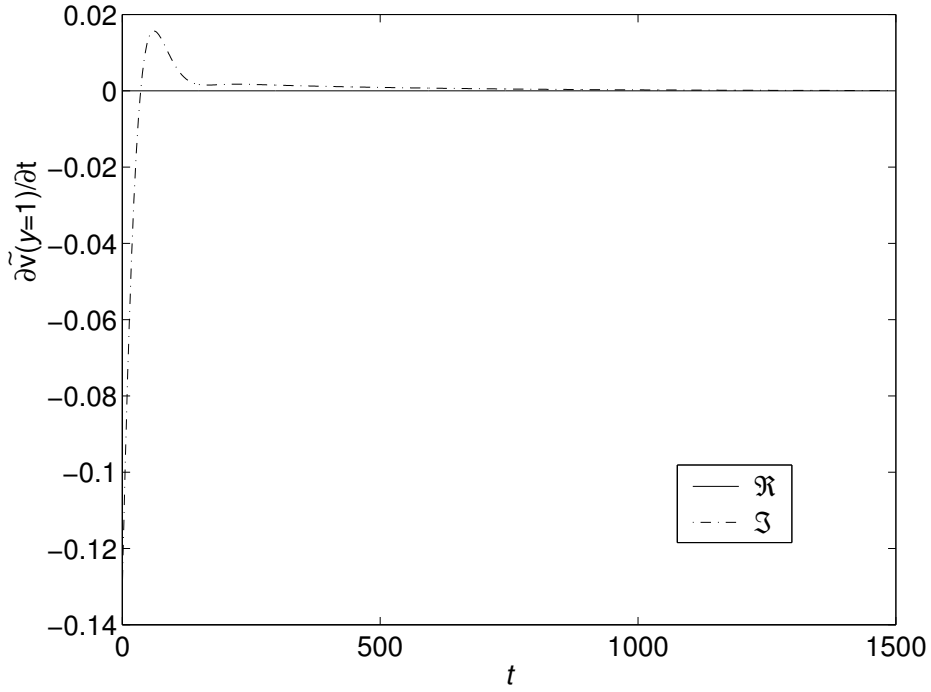

Figure 9. LQR Upper Wall Control $\mathbf{U}(1)$ vs t, from initial conditions $\mathbf{X}_{worst}$ scaled to $E = 1$, $N = 100$

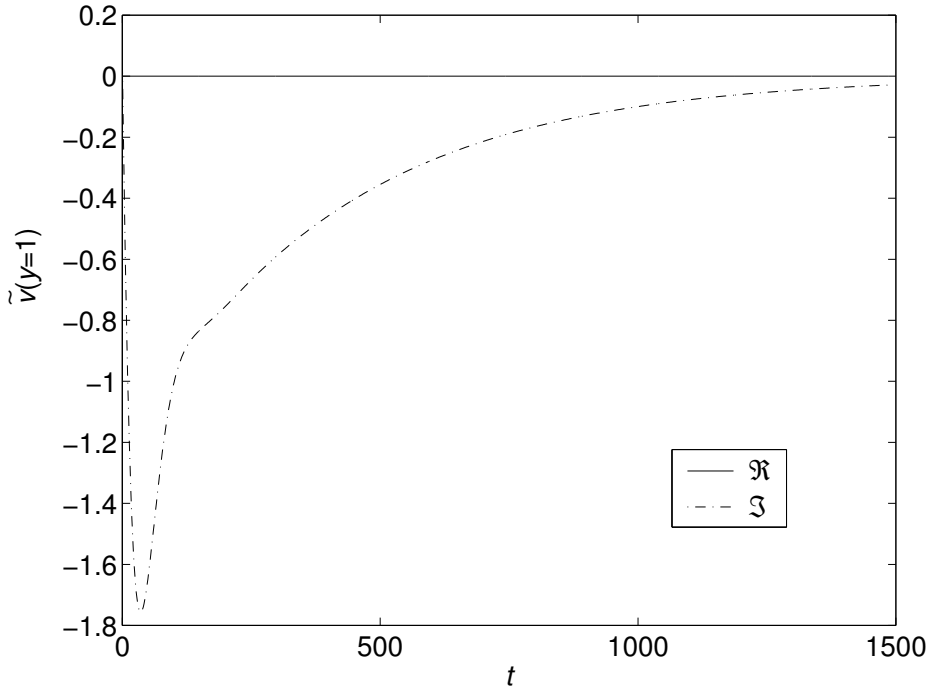

Figure 10. LQR Wall Velocity Coefficient, $\tilde{v}(y = 1)$ vs t, from initial conditions $\mathbf{X}_{worst}$ scaled to $E = 1$, $N = 100$

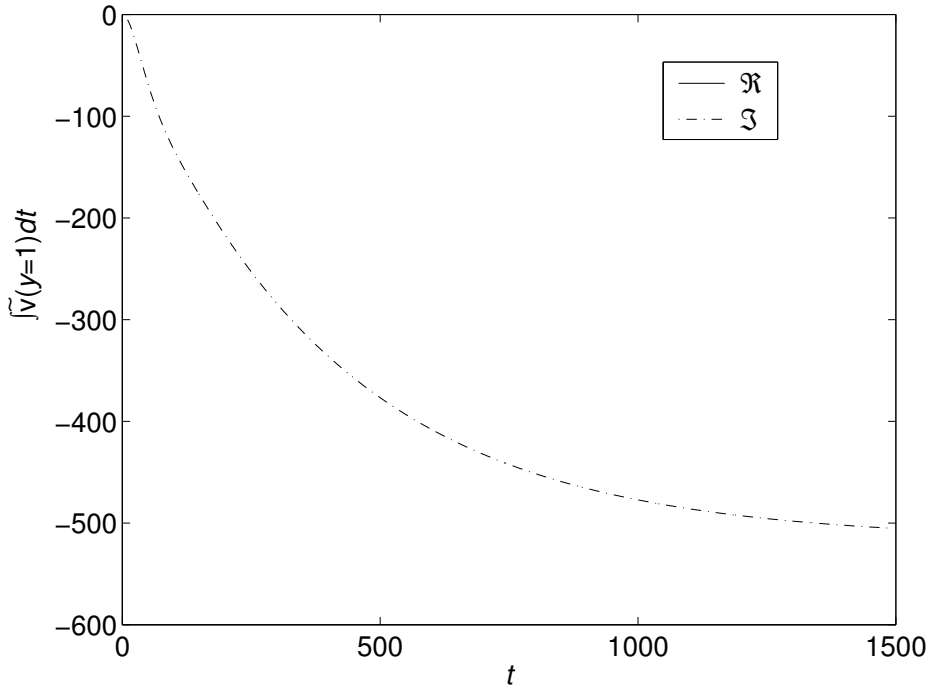

Figure 11. LQR Fluid Depth Transpired on Upper Wall vs t, from initial conditions $\mathbf{X}_{worst}$ scaled to $E = 1$, $N = 100$

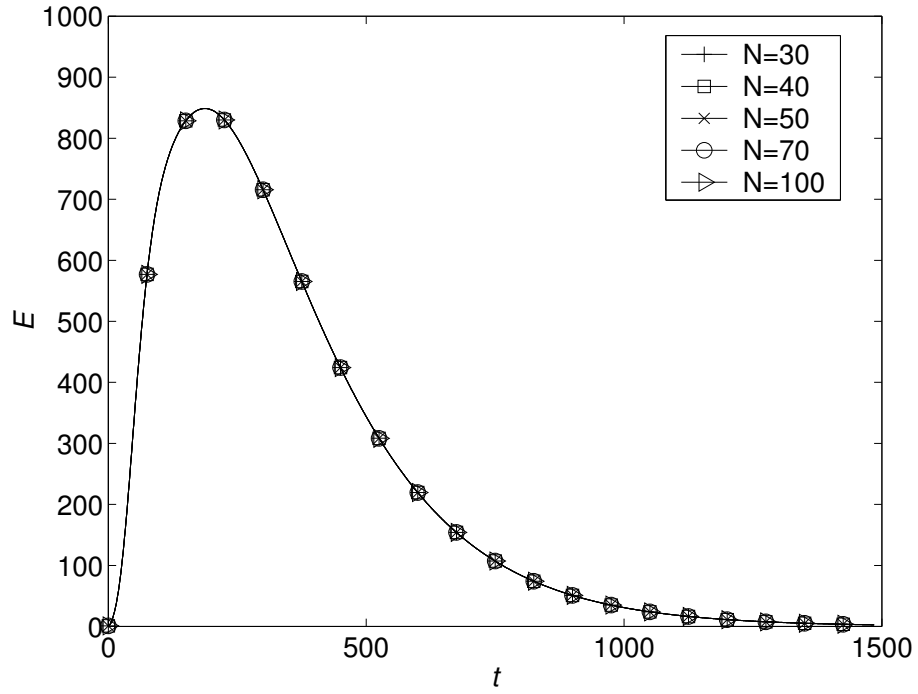

Figure 12. LQR Transient Energy E vs t, for Various Discretisations N, from initial conditions $\mathbf{X}_{worst}$ scaled to $E = 1$

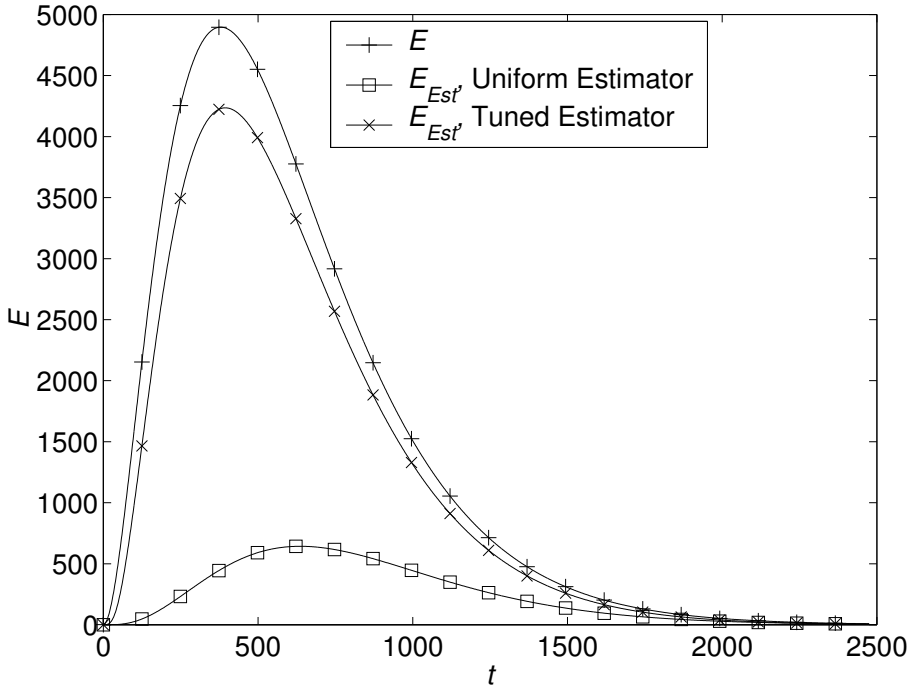

Figure 13. LQE Transient Energy E vs t, from initial conditions $\mathbf{X}_{worst}$ scaled to $E = 1$, $N = 100$

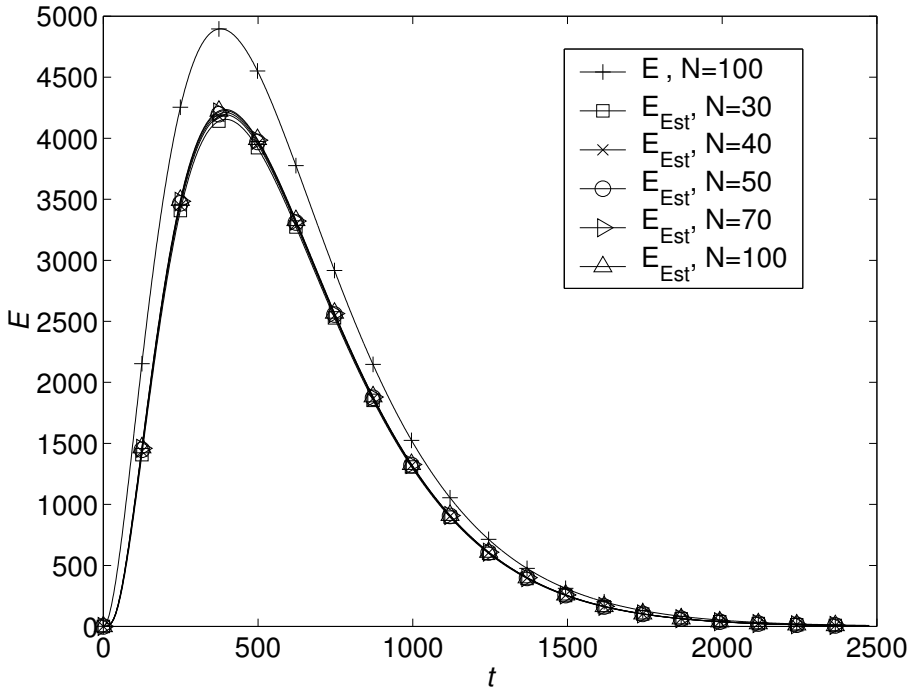

Figure 14. LQE Transient Energy E vs t, for Several Discretisations N, from initial conditions $\mathbf{X}_{worst}$ scaled to $E = 1$

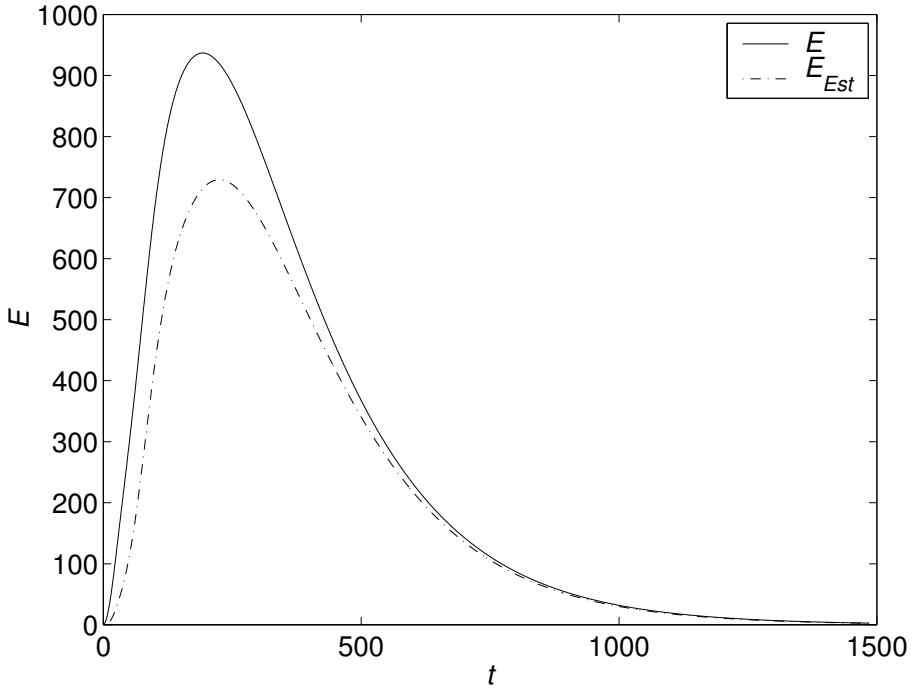

Figure 15. LQG E vs t, from initial conditions $\mathbf{X}_{worst}$ scaled to $E = 1$, $N = 100$

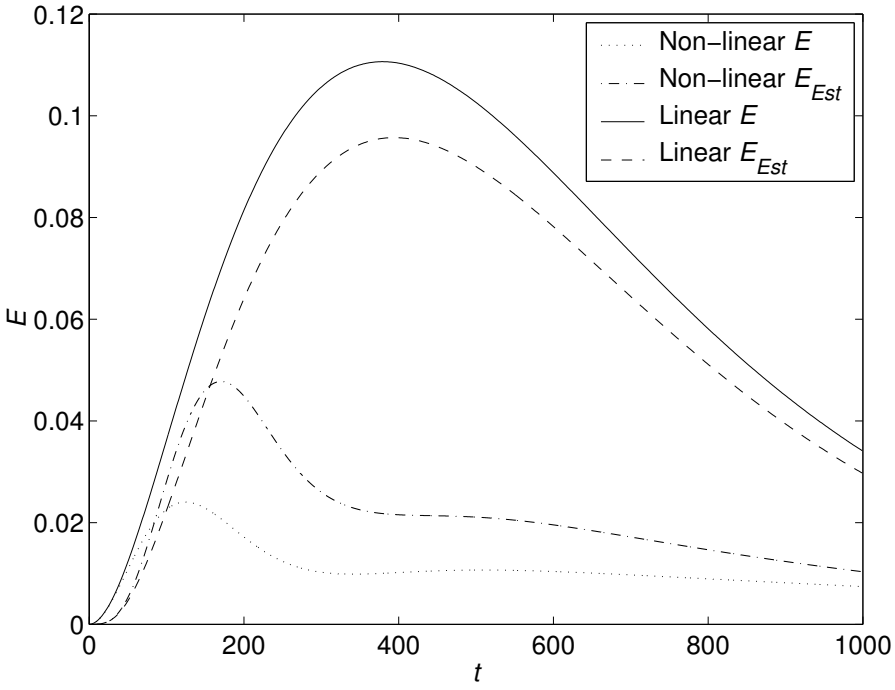

Figure 16. Open-Loop Transient Energy E vs Time t, from initial conditions $\mathbf{X}_{Worst}$ scaled to Energy $10^4 E_0$

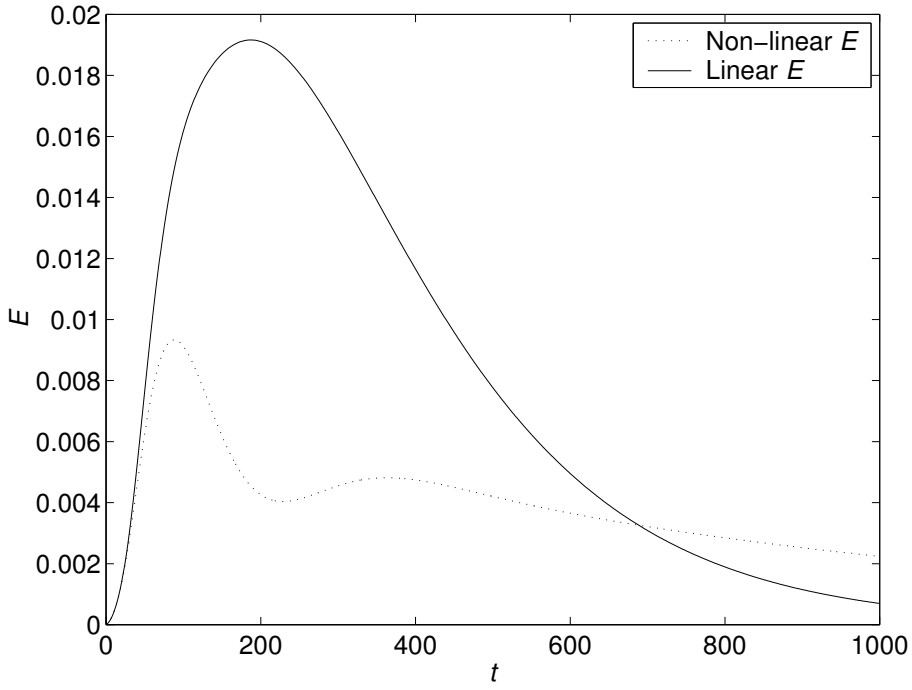

Figure 17. LQR Transient Energy E vs Time t, from initial conditions $\mathbf{X}_{Worst}$ scaled to Energy $10^4 E_0$

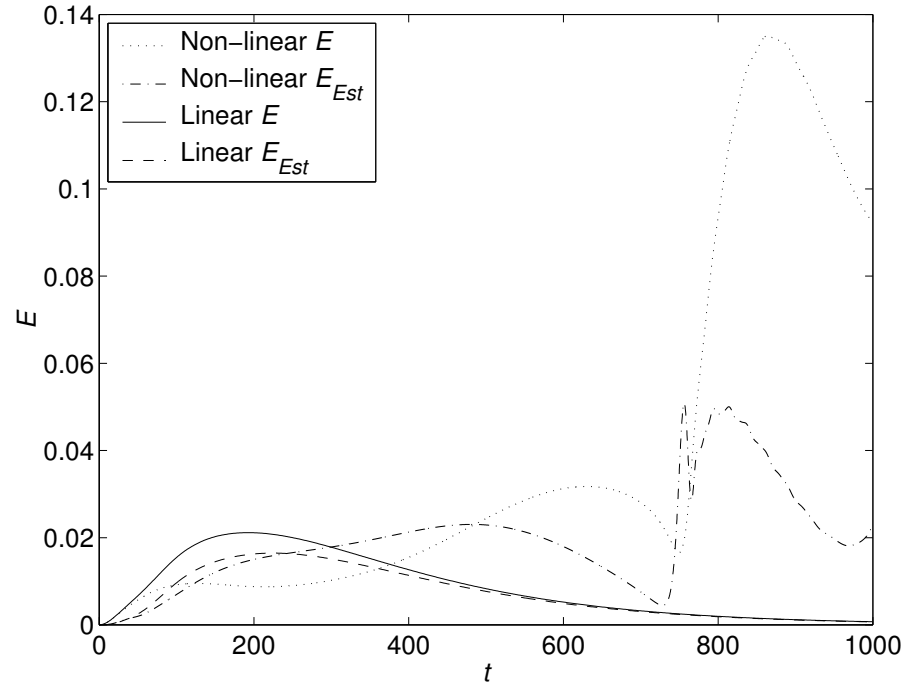

Figure 18. LQG Transient Energy E vs Time t, from initial conditions $\mathbf{X}_{Worst}$ scaled to Energy $10^4 E_0$

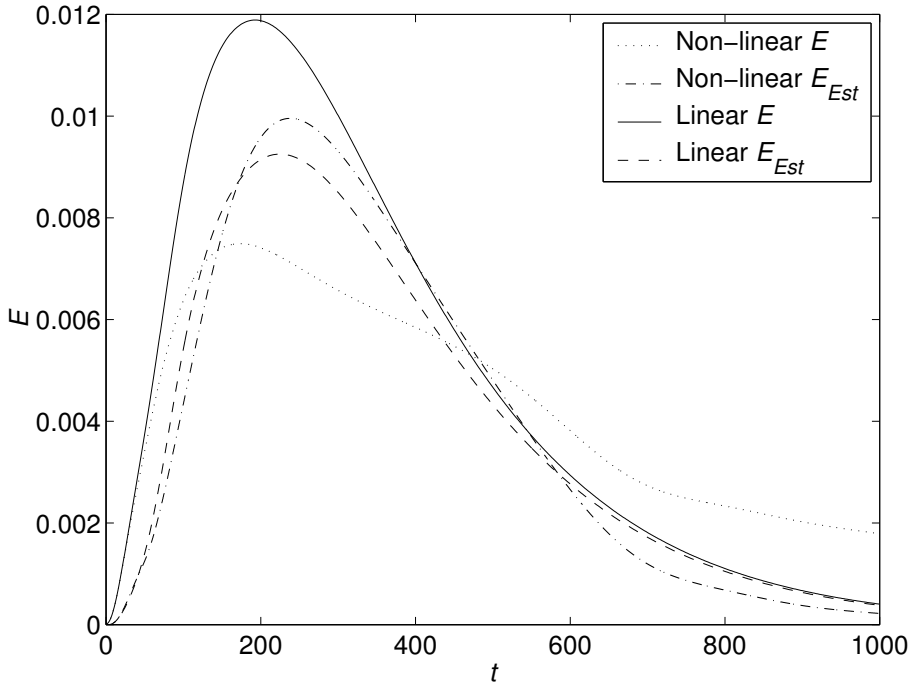

Figure 19. LQG Transient Energy E vs Time t, from initial conditions $\mathbf{X}_{Worst}$ scaled to Energy $5625E_0$

Linear quadratic control of plane Poiseuille flow-the transient behaviour.

McKernan, John

2007-12

J. Mckernan; J. F. Whidborne; G. Papadakis, Linear quadratic control of plane Poiseuille flow-the transient behaviour. International Journal of Control, Volume 80, Issue 12, December 2007, pages 1912-930.

http://dx.doi.org/10.1080/00207170701477764